

Spatially Structured Regression for Non-conformable Spaces: Integrating Pathology Imaging and Genomics Data in Cancer

Nathaniel Osher^{a,*}, Jian Kang^a, Arvind Rao^{b,c,a}, Veerabhadran Baladandayuthapani^a

^aDepartment of Biostatistics, University of Michigan, Ann Arbor, MI 48105

^bDepartment of Computational Medicine & Bioinformatics, University of Michigan, Ann Arbor, MI

^cDepartment of Radiation Oncology, University of Michigan, Ann Arbor, MI

*Corresponding author. E-mail: oshern@umich.edu

June 25, 2024

Abstract

The spatial composition and cellular heterogeneity of the tumor microenvironment plays a critical role in cancer development and progression. High-definition pathology imaging of tumor biopsies provide a high-resolution view of the spatial organization of different types of cells. This allows for systematic assessment of intra- and inter-patient spatial cellular interactions and heterogeneity by integrating accompanying patient-level genomics data. However, joint modeling across tumor biopsies presents unique challenges due to non-conformability (lack of a common spatial domain across biopsies) as well as high-dimensionality. To address this problem, we propose the Dual random effect and main effect selection model for Spatially structured regression model (**DreameSpase**). **DreameSpase** employs a Bayesian variable selection framework that facilitates the assessment of spatial heterogeneity with respect to covariates both within (through fixed effects) and between spaces (through spatial random effects) for non-conformable spatial domains. We demonstrate the efficacy of **DreameSpase** via simulations and integrative analyses of pathology imaging and gene expression data obtained from 335 melanoma biopsies. Our findings confirm several existing relationships, e.g. neutrophil genes being associated with both inter- and intra-patient spatial heterogeneity, as well as discovering novel associations. We also provide freely available and computationally efficient software for implementing **DreameSpase**.

Keywords: Bayesian variable selection, Cancer genomics, Cancer imaging, Data integration, Random effect selection

1 Introduction

1.1 Scientific motivation and background

The tumor microenvironment Tumors consist of many different components with complex interrelationships, including the vascular network within the tumor, the extracellular matrix of the tumor cells, and the immune cell composition of the tumor (Sun 2016). These structures are collectively referred to as the *Tumor Microenvironment* (TME). The TME plays a critical role in the cancer development, progression and the efficacy of certain treatments (Sadeghi Rad et al. 2021). Among its various components, the immune composition of the TME has garnered much interest among cancer researchers. This interest is due to increasing recognition of cancer’s ability to avoid destruction by the immune system as one of the organizing principles (“hallmarks”) of cancer evolution (Hanahan 2022). Briefly, the immune composition of the TME is a fractally complex ecosystem. The broad class of “immune cells” is divided into a multitude of immune cell subtypes (Zoghi et al. 2023). Sometimes subtypes of the same immune cell can even have divergent associations with prognosis (Li et al. 2021). Adding to this complexity is the variability in the spatial composition of the TME. While the prevalence of certain cell types within the TME can be informative, more recent research has shown that the relative spatial locations of different immune cell types (i.e. the tumor geography) offer insights into tumor classification and prognostic assessment (Krishnan et al. 2022).

Digital pathology The complexity of TME has spurred research in the development and application of systematic quantitative assessment and computational modeling, an area often collectively referred to as *Digital Pathology*. Digital pathology encompasses a broad array of aims and methods in the context of cancer pathology imaging, including classification of cells in the TME, determination of tumor grade, and the evaluation of spatial and morphological patterns in the tumors (Heindl et al. 2015). Given the time

and labor intensive nature of assessing the spatial composition of the TME, the focus on evaluating spatial and morphological patterns has become a central aim in digital pathology research (Baxi et al. 2022). While there are many spatial characteristics of tumors that are potentially of interest, such as the distributions of stromal cells and blood vessels within the tumor, in this paper we focus on modeling tumor-immune interaction. Our goal is to characterize the spatial configurations of tumor cells and immune cells where the two cell types tend to cluster as positively interacting, and configurations where they tend to avoid one another as negatively interacting. This spatial tendency reflects the infiltration of the tumor by immune cells.

Motivating dataset and key scientific questions The motivating imaging data for this project comes from Melanoma biopsies collected by The Cancer Imaging Archive (Clark et al. 2013). After some image preprocessing, the cell-type (i.e. phenotypes) and locations of individual cells in the biopsies are determined - see Figure 1 for examples of two such biopsies (Osher et al. 2023); additional details provided in Section 5. In addition to the high definition pathology images, bulk RNA-seq data were collected for each patient at the biopsy level. This data naturally raises three fundamental scientific questions. First, what is the appropriate method of quantification of spatial tumor-immune interactions within and between different biopsies (in other words, the extent to which immune cells interact with tumor cells)? Second, how does the variability in these interactions between biopsies relate to molecular composition of the tumor? Investigating this may shed light on the biological mechanisms most responsible for tumor-immune interactions. Third and finally, how does the variability in interaction *within* biopsies (i.e. intra-tumoral heterogeneity) relate to molecular composition of the tumor? Fundamentally, answering these three questions requires a synthesis of information from both imaging and genomics data.

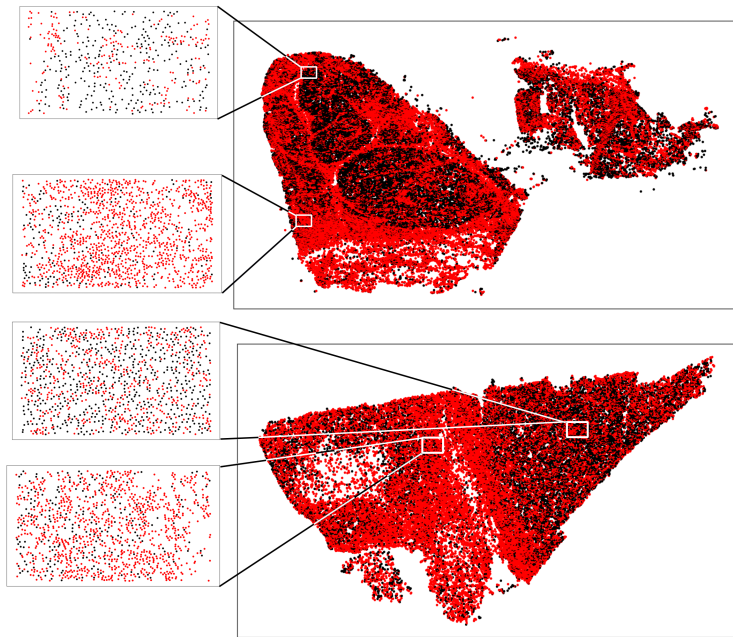


Figure 1: Plot of two biopsies from motivating Melanoma data set. Cell types and locations for two biopsies in the data set. Black points represent tumor cells, while red points represent immune cells. Enlarged portions are sub-regions with varying degrees of tumor-immune interaction.

1.2 Statistical challenges

Data structure As demonstrated by Figure 1, tumor-immune cell organization can vary considerably both within and between biopsies, which can have drastically different physical structures. Furthermore, it is of interest how these cellular interactions vary both within and between biopsies with respect to a set of covariates of interest (i.e. gene expression data). The resulting data are complex and multifaceted, yet three key aspects are particularly influential in determining the appropriate analysis approach. We refer to these aspects as the *resolution of the outcome*, the *resolution of the covariates* and the *conformability of the spaces*. The *resolution of the outcome* refers to the “level” at which the outcome of interest is observed (i.e. at the biopsy level or spatially across the biopsy), and the *resolution of the covariates* is defined analogously. Conformability refers to whether or not the spaces share a similar structure.

A great deal of work has been done in modeling of spatial data from conformable spaces that can be “mapped” to a common space, along with high-resolution outcomes

and covariates (outcomes and covariates that are observed at many spatial locations- see [MacNab 2022](#) and references there-in). Additionally, a considerable amount of work has been done on data from conformable spaces with either high-resolution outcomes and low-resolution covariates or low-resolution outcomes and high-resolution covariates, especially in the context of brain imaging data ([Bowman 2014](#) and references there-in). However, comparatively little work has been done to model spatial data from non-conformable spaces with high resolution outcomes and low resolution covariates.

The structure of our motivating data set is considerably different than those listed above. Each biopsy is partitioned into non-overlapping sub-regions, which can then be modeled using spatial point processes. Measures of interactions can then be summarized for each of the sub-regions, and modeled with respect to biopsy level covariates such as gene expression data and/or patient demographics and clinical outcomes. The result is data with high resolution outcomes, low-resolution covariates, and non-conformable spaces. While such structure poses no great obstacle to modeling heterogeneity with respect to covariates *between* patients, modeling spatial heterogeneity *within* patients with respect to covariates requires considerably more thought.

Existing methods While there are existing methods that model interactions in the TME, they largely focus on within biopsy modeling rather than joint modeling across biopsies. Most notably in the statistical domain there has been work to develop novel spatial models to assess interaction within the TME ([Li et al. 2019a](#); [Li et al. 2019b](#)). There have also been successful applications of machine learning methods to this end, focusing on the application of deep learning models and clustering ([Abousamra et al. 2022](#); [Saltz et al. 2018](#)). To our knowledge, a joint model to borrow strength across biopsies that would answer the aforementioned scientific questions of interest has not been developed. Another solution to this problem is to convert the non-conformable spatial data to functional representations, which can then be analyzed in the paradigm of functional data analysis ([Vu et al. 2022](#);

Chervoneva et al. 2021; Yang et al. 2017). While this is a viable course of action for cross-biopsy modeling, it does not take into account the inherent spatial structure and correlation between adjacent sub-regions.

1.3 Model overview

Model components In this paper, we present the Dual random effect and main effect selection model for Spatially structured regression (**DreameSpase**). As conceptually outlined in Figure 2, we first quantify the spatial interactions between tumor-immune cells through point process modeling (Panel A). Subsequently, **DreameSpase** model extends the spike and slab prior traditionally used for fixed effects to the variance terms of spatial random effects. This allows for the joint modeling of inter-biopsy heterogeneity with respect to covariates via the fixed effects, and intra-biopsy heterogeneity with respect to covariates via the spatial random effects (Panel B). The novelty of the model lies in its ability to account for heterogeneity both within and between non-conformable spaces with respect to arbitrary covariates of interest. The model consists of two components of primary interest (Panel C):

1. *Fixed effect selection component.* The model performs fixed effect selection via spike and slab priors. In the context of cancer genomics, this component accounts for the heterogeneity of the outcome of interest *between* biopsies with respect to gene expression data.
2. *Spatial random effect selection component.* In contrast to the fixed effect selection component, the random effect selection component accounts for the heterogeneity *within* biopsies with respect to gene expression data.

As we demonstrate via simulation studies, gains in selection accuracy through joint modeling of the fixed and random effects are considerable as compared to non-spatial and independent (two-step) approaches. We apply **DreameSpase** to our motivating data set

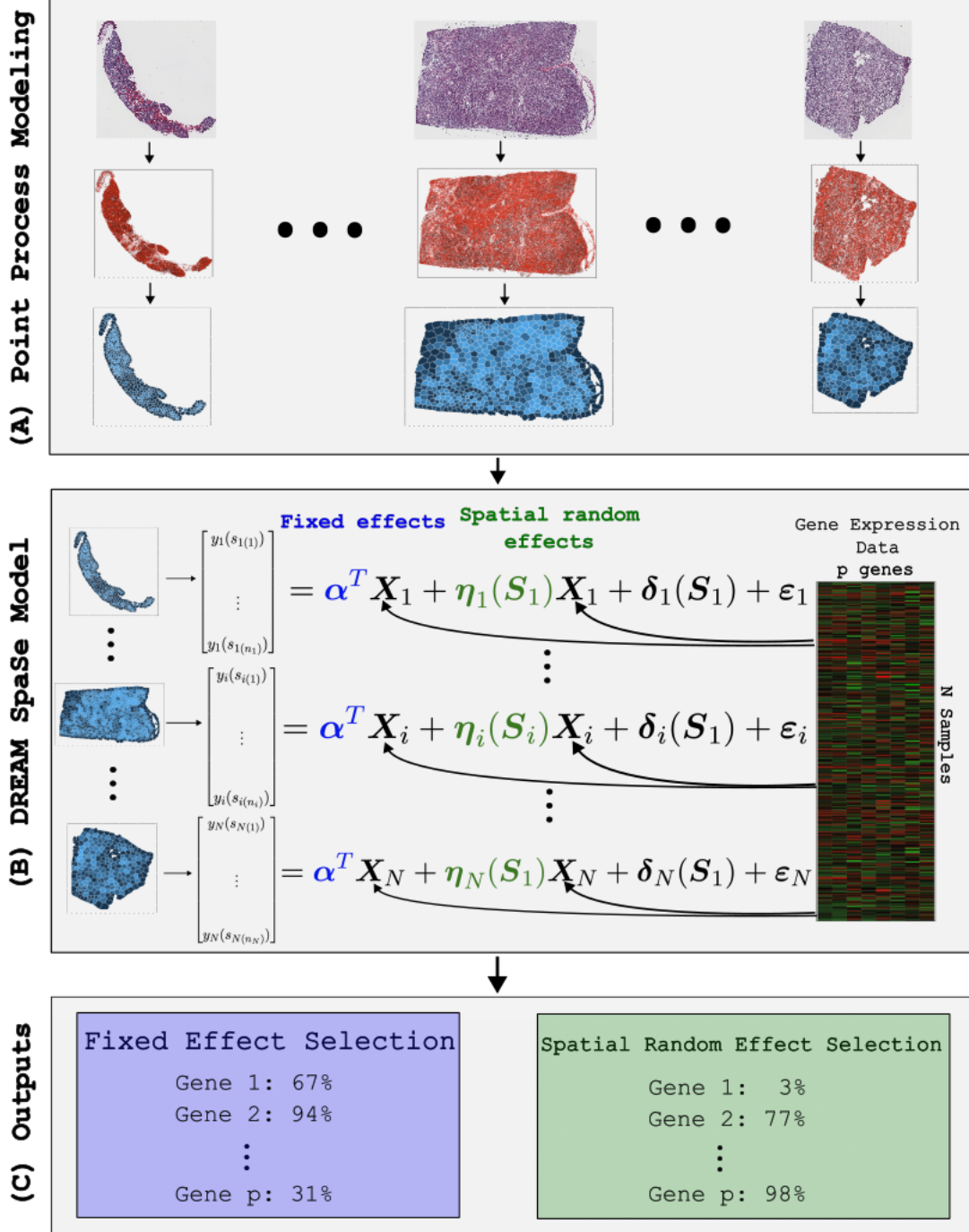


Figure 2: Overview of the DreameSpace model. (A) Point process modeling. Types and locations are determined for each cell in high definition biopsy images (top row to middle row). Biopsies are then divided into non-overlapping sub-regions, on which a measure of spatial interaction is computed (middle row to bottom row). **(B) DreameSpace model fitting.** Sub-regional outcomes are vectorized and the DreameSpace model is fit on the resulting vectors. Gene expression data, measured at the biopsy level, is used as the covariate set of interest. **(C) Fixed and Random Effect Selection.** Selection of both fixed and random effects are summarized for the model. fixed effects indicate association between covariates and average level of infiltration in a given biopsy, while random effects indicate association between covariates and heterogeneity of infiltration in a given biopsy.

consisting of 335 images and associated gene expression data for various immune classes. We find that the neutrophil class was most consistently associated with within- and between-biopsy heterogeneity of interaction between immune cells and tumor cells. The association between several neutrophil class genes were consistent with the relationships previously established in the literature, while others were suggestive of potential novel relationships.

The remainder of the paper is organized as follows. Section 2 details the formal model structure and formulation. Section 3 provides the details of the sampling algorithm and inferential summaries of interest. Section 4 outlines the simulation studies and assessments with comparative methods. Section 5 presents the results of analyzing whole slide Melanoma biopsy pathology imaging and genomic data. Finally, we conclude with discussion, limitations, and possible future directions for research in Section 6.

2 DreameSpase model

2.1 Modeling tumor-immune cell interactions

The hierarchical Strauss model In order to quantify the interaction between these two types of cells, we employ a Bayesian *Hierarchical Strauss Model* (HSM) (Höglander and Särkkä 1999). The HSM offers a parametric model that can capture both positive and negative interaction between points of different types, i.e. the tendency of the two types to either cluster towards one another or “avoid” one another. We chose the HSM for two primary reasons. First, it can capture both positive and negative interaction between different types of points, which the more standard Strauss model cannot accomplish. Second, the HSM captures the inherent biological nature of interaction between the tumor and the associated immune cells. The HSM is called “hierarchical” because the modeling of the second type of points (in our case, immune cells) is done conditionally on the locations of the first type of points (in our case, tumor cells). While the interaction between the tumor and immune cells is complex, as a first order approximation it is natural to assume as a

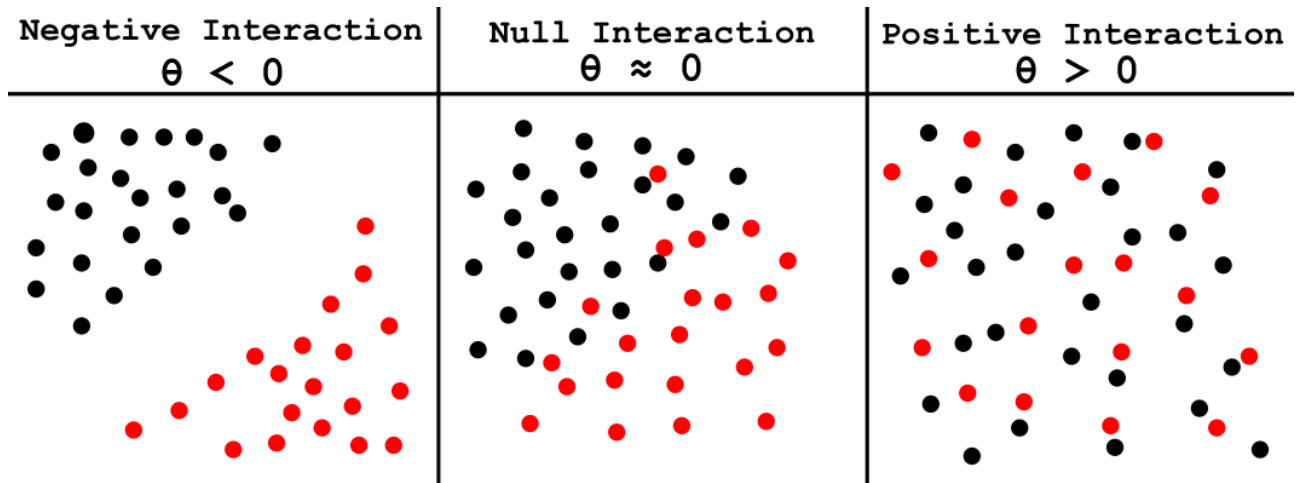


Figure 3: Illustration of interaction/co-localization. The leftmost panel illustrates low-interaction, i.e. the cells of different types do not tend to be near one another. The middle panel illustrates moderate interaction, i.e. some cells of both types tend to be near one another, while others do not. The third and final panel illustrates high interaction, i.e. the cells of both types exhibit a strong tendency to be near cells of the other type.

first order approximation that the tumor precedes the immune response, and thus it makes intuitive sense to model the immune response conditional on the locations of the tumor cells. The density of the HSM model is as follows:

$$f(\mathbf{x}_1, \mathbf{x}_2) \propto \exp \{n_1\beta_1 + n_2\beta_2 + S_R(\mathbf{x}_1, \mathbf{x}_2)\theta\},$$

where the parameters β_1 and β_2 capture the first order intensity of points for types 1 and 2, respectively (tumor and immune cells), with n_1 and n_2 representing the number of points for the corresponding type. Of key importance in this model is the interaction parameter, θ , that captures the tendency of the different types of points to exhibit positive or negative interaction. To gain some intuition as to why this is the case, first note that $S_R(\mathbf{x}_1, \mathbf{x}_2)$ counts the number of pairs of points within radius R of one another where one is of type 1 and the other is of type 2. Note that R is not a parameter that is fit, but is instead chosen prior to the model fitting based on knowledge of the particular domain being modeled. Thus, when θ is negative it “penalizing” the density put on configurations where points of the two types tend to cluster. Conversely, such configurations being “rewarded” when θ is positive. In essence, θ offers a highly interpretable summary of the spatial interaction between the different types of points:

- $\theta \in (-\infty, 0)$ indicates negative interaction (as illustrated by the leftmost panel of Figure 3), and lower values indicate more negative interaction.
- $\theta \in (0, \infty)$ indicates positive interaction (as illustrated by the rightmost panel of Figure 3), and larger values indicate more positive interaction.
- $\theta = 0$ indicates null interaction, i.e. the points are “indifferent” to points of the other type, as illustrated by the middle panel of Figure 3.

Biopsy partitioning Whole slide high-resolution pathology images of biopsies typically contain between $10^4 - 10^5$ cells. For example, in our motivating data set, the median number of cells is $\sim 50,000$, with the maximum across all biopsies $\sim 190,000$. This volume means that simply computing a spatial summary on the biopsy level is challenging. Due to the sheer size of the biopsy any given spatial feature will tend to vary across the biopsy in ways that may be important. We are primarily interested in modeling interaction (the tendency of different cells to be near each other), which is quantified on a fairly local scale ($\sim 30\mu m$) which is dictated by radius of influence of a single cell. In order to capture the heterogeneity of this interaction, we partition the biopsy into sub-regions defined by the locations of the individual tumor cells. In addition, this partitioning has the added benefit of improving the computational requirements of the HSM.

More specifically, let N be the number of biopsies, respectively denoted B_1, \dots, B_N , each $B_i \subset \mathbb{R}^2$ is further partitioned into n_i disjoint sub-regions $b_{i(1)}, \dots, b_{i(n_i)}$ with $b_{i(j)} \subseteq B_i$, $b_{i(j)} \cap b_{i(k)} = \emptyset$ for $k \neq j$, and $B_i = \bigcup_{j=1}^{n_i} b_{i(j)}$. On sub-region $b_{i(j)}$ we observe a marked point process model $\mathbf{P}_{i(j)}$ consisting of two types of points, tumor cell and immune cell.

The HSM can be fit on each of the non-overlapping sub-regions to determine the local level of tumor-immune interaction, as shown in panel A of Figure 2. For more details on the HSM and the θ parameter, see Sections S1.2 and S1.3 of the supplementary materials. The model can be fit using standard Bayesian posterior sampling methods on the so-called

pseudolikelihood function used in the estimation of these models; see Section S1.2 of the supplementary materials for model fitting details. While there are many options in the spatial statistical literature for measuring and summarizing interaction between different types of points, one of the primary advantages of θ is that it tends to be normally distributed in its posterior distribution at the level of sub-regions (Figure S1 in the supplementary materials).

At the end of this modeling step, we obtain a partition of each biopsy into non-overlapping sub-regions, and a measure of tumor-immune interaction on each of the sub-regions. Let N be the number of biopsies, denoted B_1, \dots, B_N , where biopsy B_i has n_i observed cells c_{i1}, \dots, c_{in_i} . For each c_{ij} , two pieces of information are observed: its location on the slide, $\mathbf{x}_{ij} = [x_{ij1}, x_{ij2}]$, and its type, t_{ij} , which is either “tumor” or “immune.” Next, we specify a joint model for the tumor-immune interaction across biopsies conditional on biopsy level covariates.

2.2 Spatially structured regression model

From the previous step the resulting data structure is as follows: for each biopsy B_1, \dots, B_N , suppose we observe on each biopsy B_i a continuous outcome of interest at locations \mathbf{S}_i , i.e. $\mathbf{Y}_i(\mathbf{S}_i) = [y_i(s_{i(1)}), \dots, y_i(s_{i(n_i)})]^T$. Note that in our application, $y_i(s_{i(1)})$ is the θ parameter estimated on that sub-region as described in Section 2.1. Additionally, suppose that for each biopsy, p biopsy-level covariates (in our application, gene expression data) are observed, denoted by $\mathbf{X}_i = [x_{i1}, \dots, x_{ip}]^T$. The primary motivation for our modeling is to assess whether or not the biopsy level covariates are associated at the population level with increased heterogeneity within or between biopsies. To this end, we define the DreameSpace model for biopsy $i \in \{1, \dots, N\}$ as:

$$\mathbf{Y}_i(\mathbf{S}_i) = \left(\overbrace{\boldsymbol{\alpha}^T}^{\text{Fixed effects}} \mathbf{X}_i \right) + \overbrace{\boldsymbol{\eta}_i(\mathbf{S}_i)}^{\text{Covariate specific random effects}} \mathbf{X}_i + \overbrace{\boldsymbol{\delta}_i(\mathbf{S}_i)}^{\text{Spatial random effect}} + \boldsymbol{\epsilon}_i. \quad (1)$$

We discuss each component of the model in detail below.

Fixed effects In (1), $\alpha^T \mathbf{X}_i$ is the biopsy level mean of sub-region level outcomes. Thus, α captures the variance explained by the covariates *between* different biopsies and, conditional upon the covariates, can be interpreted in expectation at a population level much like the coefficients of a standard multiple regression. The object of this component of the model is to identify covariates which are systematically associated with an increase the average level of interaction in a given biopsy.

Covariate specific random effects The term $\boldsymbol{\eta}_i(\mathbf{S}_i)$ in (1) is an $n_i \times p$ matrix of *covariate specific spatial random effects* for each biopsy. Each column of $\boldsymbol{\eta}_i(\mathbf{S}_i)$ represents a spatial random effect for a specific covariate. More concretely, denoting the j th column of $\boldsymbol{\eta}_i$ by $\boldsymbol{\eta}_{i(j)}(\mathbf{S}_i)$, we assume that $\boldsymbol{\eta}_{i(j)}(\mathbf{S}_i)$ follows a conditionally autoregressive (CAR) process. The CAR process and other models derived from it are commonly used to analyze areal data in order to share information across adjacent sub-regions (Orozco-Acosta et al. 2022). The form of the specific CAR process is given by:

$$\boldsymbol{\eta}_{i(j)}(\mathbf{S}_i) \sim MVN(\mathbf{0}, \psi_j^2 [D_w(\mathbf{W}_i) - \phi \mathbf{W}_i]^{-1}). \quad (2)$$

While other options for modeling areal data exist, the CAR prior is appealing since it makes minimal assumptions about the structure of the spatial correlation beyond the dependency of regions on their neighbors as well as the fairly small number of parameters. This is particularly appealing given the non-conformability of the underlying tumor biopsies. Under this specification, \mathbf{W}_i is an $n_i \times n_i$ symmetric matrix, where the entry in column j of row i (and column i of row j) is 1 if sub-regions i and j are adjacent, and 0 otherwise; $D_w(\mathbf{W}_i)$ is a diagonal matrix where each diagonal entry is the sum of the corresponding row of \mathbf{W}_i ; ψ_j^2 captures the variability of the value in a sub-region conditional upon the value of its neighbors; and ϕ captures the spatial correlation between neighbors. Note that while ϕ takes on values in $(-1, 1)$ and determines the correlation between adjacent sub-regions

under this model specification, it is not itself *equal* to the correlation between adjacent sub-regions. The distribution of this spatial random effect is thus determined by the values of ψ_j^2 and ϕ .

The key parameter when considering the covariate specific spatial random effects is ψ_j^2 . This parameter affects the outcome via the multiplication between the matrix of random effects and the covariate vector. Consider, as an extreme but illustrative example, the case where $\psi_j^2 = 0$. When this is the case, we should expect no systematic change heterogeneity *within* a biopsy as the j th covariate changes, as each $\boldsymbol{\eta}_{i(j)}(\mathbf{S}_i)$ has a degenerate distribution at $\mathbf{0}$. However, consider $\psi_j^2 > 0$. As the magnitude of x_{ij} increases, we should in turn expect to see a systematic increase in the heterogeneity of biopsy i . Note that this may not translate to an increase in the average *level* of heterogeneity in biopsy i - whether or not such an increase occurs depends on the value of α_j . These two examples, while extreme, embody the logic underlying our decision to use spike and slab priors to regularize the fittings of these parameters; details deferred to Section 2.3 for now.

Global CAR process In (1), $\boldsymbol{\delta}_i(\mathbf{S}_i)$ is the “global” spatial random effect that captures the overall spatial correlation across all biopsies. We assume that that $\boldsymbol{\delta}_i(\mathbf{S}_i)$ follows an analogous CAR process, defined as:

$$\boldsymbol{\delta}_i(\mathbf{S}_i) \sim MVN(\mathbf{0}, \tau^2 [D_w(\mathbf{W}_i) - \rho \mathbf{W}_i]^{-1}),$$

where each term is defined analogously to its counterpart in (2). Like the covariate specific CAR process, the distribution of this spatial random effect is thus determined by the values of τ^2 and ρ . However, unlike the covariate specific CAR process, the ρ parameter is estimated. While the model is well-defined for $\rho \in (-1, 1)$, values less than zero indicate *anti*-correlation between neighbors. Because this is not a priori biologically plausible (there is no reason to suspect that adjacent tumor sub-regions should differ systematically), we assume that $\rho \in [0, 1)$, i.e. that sub-regions are on average either positively correlated or

independent of their neighbors.

Pure error Finally, the $\epsilon_i \sim MVN(\mathbf{0}, \nu^2 \mathbf{I})$ is the pure error of the model (often referred to as the “nugget”), i.e. the error that is not accounted for by the fixed effects, the global CAR process, or the covariate specific CAR processes.

It should be noted that the `DreameSpace` model is agnostic to how the values on the sub-regions are generated; nothing about the downstream model depends on the usage of point processes to generate sub-regional outcome measurements. The only assumption is that the outcomes observed at the level of each sub-region are spatially correlated and (approximately) normally distributed.

2.3 Dual main and random effect spatial selection

Motivation A challenge of working with genomic data is the dimensionality. Even when utilizing a targeted subset of available genes, it is neither likely nor expected that all genes included in the model are meaningfully related to the outcome. This necessitates some degree of selection or regularization in order to properly determine which genes are significantly associated with the outcome of interest. Performing selection yields the dual benefits of producing a more parsimonious model while also improving the accuracy of parameter estimates. To accomplish this in the context of our model, we utilize spike and slab priors for both the fixed and random effects. We focus discussion on these priors due to their importance in the model.

Spatial fixed effects While there are several ways to parameterize a spike and slab prior, our method represents a standard application of *stochastic search variable selection* ([George and McCulloch \(1993\)](#)). The prior is specified for each entry of the fixed effect vector α_j as follows:

$$\alpha_j \sim \gamma_j N(0, \sigma_{slab}^2) + (1 - \gamma_j) N(0, \sigma_{spike}^2),$$

$$\gamma_j \sim \text{Bernoulli}(P_\gamma),$$

where P_γ is the prior probability of inclusion for the fixed effects and is assumed to come from a common (non-informative) $Beta(1, 1)$ prior distribution. Note that under our specification, as is often the case, σ_{spike}^2 and σ_{slab}^2 are not *estimated*, but rather selected *a priori*; in our application, we set $\sigma_{spike}^2 = 0.03$ and $\sigma_{slab}^2 = 100$. This prior construction allows not only the estimation of each α_j via the posterior mean, but also the probability of inclusion in the model via the posterior mean of the γ_j parameter. Because γ_j is an indicator, the posterior expectation corresponds to the probability that $\gamma_j = 1$, which is the probability that α_j is included in the model (i.e. is not penalized by the prior).

Spatial random effects Unlike standard fixed effect coefficients, variance terms are constrained by definition to lie in the range $[0, \infty)$. The challenge in adapting the spike and slab prior to the variance terms of random effects stems from the difference in domains between the variance terms $\psi_1^2, \dots, \psi_p^2$ and the fixed effect terms $\alpha_1, \dots, \alpha_p$. In theory each fixed effect term can take on any value in \mathbb{R} , even if excessively large or small values are implausible in practice. This is not the case when dealing with variance parameters. By definition, such parameters must lie in $[0, \infty)$. This rules out the usage of normal priors centered at zero, which put half their mass in the range $(-\infty, 0]$. Because of this asymmetry, various models have been constructed by utilizing specialized Cholesky decompositions of the covariance matrix of the random effect terms (Joyner et al. 2020; Ibrahim et al. 2011). By placing penalties (in the form of priors or regularization components) on terms in the decompositions of the covariance matrix rather than directly on the terms of the covariance matrix, these models avoid dealing with both the constraints of covariance matrices as well as the domain restrictions of variance terms. As a result, such penalties can be constructed in the same manner as they might for more standard fixed effect terms. Others, such as Scheipl et al. 2012, employ a spike and slab formulation on variance terms in the context of structural additive regression (STAR) models. However, the form and purpose of this model differs considerably from our own, as the purpose of STAR models is to provide a

flexible and generalizable method for modeling the mean of some outcome vector.

We define the “*half-spike* and *half-slab*” priors for the variance terms using half-normal distributions as follows:

$$\psi_j^2 \sim d_j N^+(0, \xi_{slab}^2) + (1 - d_j) N^+(0, \xi_{spike}^2),$$

$$d_j \sim \text{Bernoulli}(P_d),$$

where $P_d \sim \text{Beta}(1, 1)$ is the prior probability of inclusion for all random effects. Like those of the fixed effects, the half spike is parameterized by a small variance, ξ_{spike}^2 , while the slab is parameterized by a larger variance, ξ_{slab}^2 . Half-normal distributions were used in place of more standard inverse gamma distributions partially due to the relatively larger amount of mass placed on extreme values by the half-normal and to achieve greater congruence between the fixed effect selection component of the model and random effect selection component of the model. This congruence makes it more straightforward to tune the selection of both the fixed and random effects in the model. The d_j indicator variable also serves a similar function to the γ_j in the fixed effect formulation.

Table 1: Full specification of DreameSpace model and priors. Model specification is given for N biopsies with p covariates of interest. Across all terms, i indexes the biopsy and j indexes the covariate where relevant. $\boldsymbol{\eta}_{i(j)}$ is the j th column of the $n_i \times p$ matrix $\boldsymbol{\eta}_i$, the matrix of covariate specific random effects for biopsy i .

$\mathbf{Y}_i \mid \boldsymbol{\mu}_i, \nu^2$	\sim	$MVN(\boldsymbol{\mu}_i, \nu^2 \mathbf{I}),$	$i = 1, \dots, N$
$\boldsymbol{\mu}_i$	$=$	$(\boldsymbol{\alpha}^T \mathbf{X}_i) \cdot \mathbf{1} + \boldsymbol{\delta}_i(\mathbf{S}_i) + \boldsymbol{\eta}_i(\mathbf{S}_i) \mathbf{X}_i$	$i = 1, \dots, N$
$\alpha_j \mid \gamma_j, \sigma_{spike}^2, \sigma_{slab}^2$	\sim	$\gamma_j N(0, \sigma_{slab}^2) + (1 - \gamma_j) N(0, \sigma_{spike}^2),$	$j = 1, \dots, p$
$\boldsymbol{\delta}_i(\mathbf{S}_i) \mid \tau^2, \rho, \mathbf{W}_i$	\sim	$MVN(\mathbf{0}, \tau^2 [D_w(\mathbf{W}_i) - \rho \mathbf{W}_i]^{-1}),$	$i = 1, \dots, N$
$\boldsymbol{\eta}_{i(j)}(\mathbf{S}_i) \mid \psi_j, \phi, \mathbf{W}_i$	\sim	$MVN(\mathbf{0}, \psi_j^2 [D_w(\mathbf{W}_i) - \phi \mathbf{W}_i]^{-1})$	$i = 1, \dots, N; j = 1, \dots, p$
$\psi_j \mid d_j, \xi_{spike}^2, \xi_{slab}^2$	\sim	$d_j N^+(0, \xi_{slab}^2) + (1 - d_j) N^+(0, \xi_{spike}^2)$	$j = 1, \dots, p$
ν^2, τ^2	\sim	$\text{Inverse Gamma}(0.001, 0.001)$	
ρ	\sim	$\text{Discrete}(v_1, \dots, v_K, p_1, \dots, p_K)$	$v_\ell \in [0, 1]; p_\ell \in [0, 1]; \sum_{\ell=1}^K p_\ell = 1$
$\gamma_j \mid P_\gamma$	\sim	$\text{Bernoulli}(P_\gamma),$	$j = 1, \dots, p$
$d_j \mid P_d$	\sim	$\text{Bernoulli}(P_d),$	$j = 1, \dots, p$
P_γ, P_d	\sim	$\text{Beta}(1, 1)$	

Additional priors The remaining priors in the model are generally chosen to be standard conjugate priors, with the exception of the ρ parameter. ρ is given a discrete distribution $P(\rho = v_i) = p_{v_i}$ for $i \in \{1, \dots, K\}$; see Section 3.1 for details. As a brief point of discussion, we have chosen a non-informative $Beta(1, 1)$ prior for the prior selection probabilities for the fixed and random effects, this prior could instead be assigned uniquely to each selection probability and parameterized based on prior clinical information on the importance of each covariate in the style of Ni et al. 2019. For full prior specifications, see Table 1.

3 Posterior inference

3.1 Key full conditional distributions

We perform posterior inference via Markov Chain Monte Carlo on the full parameter set outlined above: fixed effects $\boldsymbol{\alpha}$, corresponding selection indicators $\boldsymbol{\gamma} = [\gamma_1, \dots, \gamma_p]^T$, and overall probability of selection P_γ ; random effect variance terms $\boldsymbol{\psi} = [\psi_1^2, \dots, \psi_p^2]$, corresponding selection indicators $\boldsymbol{d} = [d_1, \dots, d_p]^T$, and overall probability of selection P_d ; the global CAR process parameters τ^2 and ρ ; and the pure error variance ν^2 . In this section we outline the derivations of selected full conditional distributions necessary for the implementation of the Gibbs sampling algorithm. While many of the full conditional distributions utilize conjugate or otherwise standard priors, there are several prior specifications that result in full conditional distributions unique to our model. See Table 1 for the full model specification from which all full conditional distributions can be derived, and Section S3.3 for detailed derivations of all model parameters. Due to identifiability constraints, ϕ is fixed a priori at a relatively small value (0.3).

Spatial random effects The full conditional of ψ_j^2 is induced via the prior on ψ_j , and requires somewhat more careful derivation. Specifying a half-normal prior on ψ_j causes the full conditional distribution of ψ_j^2 to be that of a *generalized inverse Gaussian* distribution. For a detailed derivation of this fact, see Section S3.3.2 of the supplementary materials.

Thus, while the prior is specified in terms of the standard deviation ψ_j , in practice the sampling is performed on the variance ψ_j^2 . However, due to the simple monotonic relationship between the two quantities, this does not pose any practical inconvenience.

Global CAR process correlations In order to improve the computational efficiency of sampling, a grid prior was placed on the correlation of the global CAR process, ρ . This prior is specified by a discrete set of values and corresponding probabilities, v_1, \dots, v_K , and p_1, \dots, p_K (full conditional distributions provided in Supplementary Section S3.3.3). In practice, sampling from this distribution is accomplished using the Gumbel Max trick (Huijben et al. 2023); see Supplementary Section S3.1 details and derivation.

3.2 Inferential summaries of interest

There are two primary inferential summaries of interest: the sub-region level summaries of interaction which are summarized within and across biopsies, and the selection probabilities for the fixed effects and random effects. While we are primarily interested in the former only as the object of modeling in this paper, these summaries can be explored in many ways in their own right. As for the latter, the usage of spike and slab priors allows for the computation of posterior probabilities of selection for both the fixed and random effects \mathbf{d} and $\mathbf{\Gamma}$, illustrated in panel C of Figure 2. For each covariate, any combination of the corresponding fixed and random effect can be selected for inclusion in the model as explained in Section 2.3. In the context of our application:

- $P(\gamma_j = 1)$ is the probability that the j th fixed effect is included in the model, indicating that the corresponding gene is associated with heterogeneity *between* biopsies
- $P(d_j = 1)$ is the probability that the j th random effect is included in the model, indicating that the corresponding gene is associated with heterogeneity *within* biopsies

If both the fixed and random effects are selected, then a given gene is associated with both inter- and intra-biopsy heterogeneity, and thus may be of particular interest.

4 Simulation studies

Simulation overview In order to assess the overall performance of our `DreameSpase` model we performed a series of simulation studies. In terms of design parameters, the number of biopsies N was fixed at 200 (on the same order as a real data example), while the number of covariates p was varied between 50, 75, and 90 to achieve ratios of $2p/N$ of 0.5, 0.75, and 0.9. We refer to the ratio $2p/N$ as the *relative dimensionality* of a setting. All covariates were generated from a standard normal distribution. The number of true fixed and random effects for each of the three settings was fixed at 3, 6, and 9, respectively. Each biopsy was simulated as a 5×5 lattice across all settings. Fixed and random effects were simulated with equal frequency to be small, medium, or large. Small, medium, and large fixed effects were simulated uniformly in the respective ranges $(0.13, 0.23)$, $(0.23, 0.33)$, and $(0.33, 0.43)$, while the corresponding ranges for random effect variance were $(0.1, 0.2)$, $(0.2, 0.3)$, and $(0.3, 0.4)$. 50 data sets were simulated for each data setting.

Comparative methods In addition to the `DreameSpase` model, two additional models were fit to serve as performance benchmarks. The first model is a special case of the `DreameSpase` model that uses non-spatial random effects. This is equivalent to setting $\phi = 0$ and $\mathbf{W}_i = \text{diag}(1, \dots, 1)$ in Equation 2. This ignores the spatial structure of the biopsy and instead models the $\boldsymbol{\eta}_{i(j)}$ as simply clustered data. As in the true model effects were selected if their estimated posterior probability of inclusion was greater than 0.5 in accordance with the median-probability selection model (Barbieri and Berger 2004). We refer to this model as the “Non-Spatial `DreameSpase`” model, abbreviated to NSDS.

The second method was a penalization-based method that a researcher might use to answer the questions posed in this paper without developing a novel method, which we refer to as the “analyst model.” There were two stages of analysis for this model: one for the fixed effect component, and one for the random effect selection component. For

the fixed effect selection component, a lasso regression was fit using the sub-region level outcomes as the outcome and the biopsy level covariates as the covariates. A penalization parameter was selected via three-fold cross validation, and fixed effects were considered to be selected if their parameter estimates were non-zero. To perform random effect selection, a lasso regression was fitted treating the standard deviation of each biopsy as the outcome, and the absolute value of the covariates as the regressors. In this case as well the penalization parameter was chosen via three-fold cross validation, and non-zero covariates were considered to be selected.

Evaluation criteria The primary goal was to assess selection accuracy of the different models and methods. To do so, the true positive rate and false positive rate of selection were computed for the fixed effects as well as the random effects. The true positive rate is computed by the size of the effects, while the false positive rate is presented across all effect sizes (since null effects do not have sizes).

Signal to noise ratio In order to properly calibrate the simulation studies to the real data and compare across differing settings, it is useful to define a signal to noise ratio. Note that unlike many models, we are interested in accurately estimating not only the fixed effect terms, but random effect terms as well. Because the two components of the model are independent of one another, we define separate signal to noise ratios for both components of the model. The fixed and random effect SNRs are defined as

$$SNR_{fixed} = \frac{\text{var}(\mathbf{X}^T \boldsymbol{\alpha})}{\text{var}(\mathbf{Y})}, \quad SNR_{rand} = \frac{\sum_{j=1}^n \text{var}(\boldsymbol{\eta}_j, \mathbf{X})}{n \text{var}(\mathbf{Y})}.$$

See Section S2.1 for details and derivations for both quantities. The chosen simulation settings yielded simulations with fixed effect SNRs in the range $[0.37, 0.42]$, and random effect SNRs in the range $[0.38, 0.39]$.

Results Table 2 shows the detailed results of the true positive rates across the effect sizes and relative dimensionality and Table 3 shows for results of the false positive rates.

Across all settings, the false positive rate of the `DreameSpase` model never exceeded 0.02. For medium and large effect sizes, the true positive rates for the fixed effects are uniformly 1.0, i.e. perfect selection. For the random effects, the true positive rate lies between 0.8 and 1.0, with the median for these effect sizes being 0.98. The model struggles substantially more with smaller effect sizes, with the lowest true positive rate obtained being 0.44 when $2p/N = 0.9$. Still, this is only marginally worse than the analyst model, which achieved the best true positive rate for this setting at 0.53. Thus, while the model may not be sufficiently sensitive to detect all effects of this magnitude, the highly controlled false positive rate means that one can be confident that the effects we do find are true effects. Moreover, while `DreameSpase` is sometimes outperformed in selection of the smallest magnitude effects by the other methods, the differences in performance are generally quite small, while the deficiencies of the other methods across the different effect types and sizes are generally quite substantial.

The analyst model was able to select random effects with reasonable accuracy, and in fact outperforms `DreameSpase` as well as the NSDS model in the $2p/N = 0.9$ setting in terms of true positive rate, consistently achieving the best selection across several settings. The lowest true positive rate for random effect selection achieved is 0.56, (which is still the best across all three models at this setting), while the highest is 1.0. The false positive rate is also well controlled for random effects, again never exceeding 0.02.

However, the failure to jointly model fixed effects and random effects resulted in a severely diminished true positive rate and inflated false positive rate for the fixed effects not seen when using the `DreameSpase` model. Because of the failure to jointly model the different effect types, the true positive rate for fixed effects lay between 0.4 and 0.56. Additionally, the false positive rate lay between 0.21 and 0.24, while `DreameSpase` and

Table 2: True positive rate (TPR) across settings, models, and effect sizes. Relative dimensionality is defined as $2p/N$, where N is the number of biopsies and p is the number of covariates. The number of covariates is doubled in the ratio to account for the estimation of both fixed effects and covariate specific random effects, thus doubling the effective dimensionality. Effect sizes refer to the magnitude of the fixed and random effects. For exact ranges, see Section 4. Bolded values indicate the best performance for a given setting and effect size. In the case of a tie, all values are bolded.

TPR $2p/N$	Effect Size	Fixed Effects			Random Effects		
		“Analyst Model”	NSDS	DreameSpase	“Analyst Model”	NSDS	DreameSpase
0.5	Small	0.56	1.00	1.00	0.94	0.98	0.98
	Medium	0.46	1.00	1.00	1.00	1.00	1.00
	Large	0.4	1.00	1.00	1.00	1.00	1.00
0.75	Small	0.48	0.63	0.61	0.76	0.26	0.76
	Medium	0.54	1.00	1.00	0.99	0.75	0.96
	Large	0.51	1.00	1.00	1.00	0.93	1.00
0.9	Small	0.53	0.44	0.44	0.56	0.05	0.53
	Medium	0.51	1.00	1.00	0.93	0.12	0.8
	Large	0.49	1.00	1.00	0.99	0.2	0.93

NSDS achieved false positive rates of less than 0.01. The only exception to this trend is the true positive rate among small effects in the $2p/N = 0.9$ setting, where the analyst model achieves a true positive rate of 0.53 compared to 0.44 for both the DreameSpase as well as the NSDS model.

For fixed effects, the performance of the NSDS model is comparable to that of DreameSpase across all settings in terms of both TPR and FPR. For random effects, however, the true positive rate of the NSDS model is similar to that of DreameSpase in the $2p/N = 0.5$ setting, but deteriorates quickly across the larger settings, at times reaching as low as 0.05. Notably, in the $2p/N = 0.9$ setting, the maximum true positive rate for random effects achieved by the NSDS model across all effect sizes is 0.2, compared to 0.93 for the DreameSpase model and 0.99 for the analyst model. While it achieves a false positive rate of virtually 0 in this setting, the DreameSpase and analyst models both achieve a modest false positive rate while also achieving a substantially higher true positive rate across all effect sizes. This indicates the importance of accounting for the spatial structure of the biopsies for the random effects.

Additional simulation results We also computed threshold free metrics, in particular Area under the curve (AUC) for all the methods and the results are shown in Table S1 of the supplementary materials. The results are broadly consistent with the ones presented

Table 3: False positive rate (FPR) across settings and models. Relative dimensionality is defined as $2p/N$, where N is the number of biopsies and p is the number of covariates. The number of covariates is doubled in the ratio to account for the estimation of both fixed effects and covariate specific random effects, thus doubling the effective dimensionality. Note that false positive rates are determined solely by the selection results for the simulated null covariates, and thus the FPR does not vary when broken down by effect size. Bolded values indicate the best performance for a given setting and effect size. In the case of a tie, all values are bolded.

FPR $2p/N$	Fixed Effects			Random Effects		
	“Analyst Model”	NSDS	DreameSpase	“Analyst Model”	NSDS	DreameSpase
0.5	0.24	< 0.01	< 0.01	< 0.01	< 0.01	0.02
0.75	0.22	< 0.01	< 0.01	0.01	< 0.01	0.01
0.9	0.21	< 0.01	< 0.01	0.02	< 0.01	0.01

above; the analyst model tends to perform well in random effect selection (normalized AUC ranging from 0.92 to 1), but struggles to a significant degree in main effect selection (normalized AUC ranging from 0.47 to 0.51).

5 Tumor microenvironment in melanoma

5.1 Background

Melanoma and immunotherapy Melanoma is a particularly interesting type of cancer given its high immunogenicity caused by its high mutational load (Marzagalli et al. 2019). This characteristic has implications not only for patient prognosis, but also susceptibility to treatment via immunotherapies (Kang et al. 2020; Simiczyjew et al. 2020). While remarkably effective in certain patients, immunotherapy is by no means a silver bullet in the treatment of melanoma. Ipilimumab, the first CTLA-4 inhibitor approved by the FDA for treatment of melanoma patients, has demonstrated remarkable efficacy in the treatment of even advanced stage melanoma, both alone and in concert with other treatments. However, the objective response rate across these different settings is far from 100% across all patients (Chesney et al. 2018). Further complicating this picture is the fact that the composition of TME has also been shown to be associated with response to immunotherapies (Falcone et al. 2020). The biological understanding of the interplay between immunotherapy and the composition of the TME has been bolstered recently by the proliferation of single cell

imaging technologies (Xiao et al. 2022). Still, more work is required to synthesize our understandings of immunological mechanisms in melanoma and its relationship to the spatial composition of the TME. To this end, we investigate the relationship between spatial composition of the TME (using pathology imaging data) and immunological mechanisms (using genomic data), both at the level of tumor-immune interactions as well as the heterogeneity of the interactions within and across tumors.

Description of pathology imaging and genomic data Our motivating imaging dataset comes from the The Cancer Imaging Archive (Clark et al. 2013), a companion consortium to the The Cancer Genome Atlas project (TCGA). TCGA is an initiative that makes available high quality genomics and imaging data on samples from a diverse range of cancer types (Weinstein et al. 2013). This multi-platform data includes, most notably for our purposes, high definition images of the biopsies and gene expression data from patient samples. Our pathology imaging data set consisted of whole slide imaging data for 335 biopsies from the Skin Cutaneous Melanoma (SKCM), with the number of cells per biopsy ranging from 814 to 187,521. The cells of each biopsy were processed and classified by a machine learning model as either tumor or immune according to the morphology of each cell. Biopsies were subsequently partitioned into non-overlapping sub-regions, and an estimate of interaction was computed for each sub-region. For more details on the cell classification algorithm and tumor partitioning algorithm, see Osher et al. (2023).

In order to determine the association between immunological mechanisms and spatial association of tumor cells and immune cells, we used gene expression data from genes associated with different groups of immune cells. These immune groups include “marker” genes linked to B cells, macrophages, monocytes, neutrophils, natural killer cells, plasma cells, and T cells. These immune cell groups regulate many important oncogenic processes such as angiogenesis, metastasis, and the response to drugs or immunotherapy (Nirmal et al. 2018).

Using the sub-regional interaction parameter estimates described in Section 2.1 as the outcome, the `DreameSpace` model was fit using gene expression data for the previously described sets of genes downloaded from the UCSC Xena browser (Goldman et al. 2020). In total, there were 11,202 sub-regions on which interaction was estimated across 335 biopsies, with the median number of sub-regions per biopsy being 29 (IQR 26). After pre-processing, there were 122 genes included in our final analysis and additional pre-processing details are available in Section S3.2 of the supplementary materials; see Algorithm S1 for the exact algorithm used.

The `DreameSpace` model was run for 300,000 total iterations, 150,000 of which were treated as burn-in. The resulting samples were thinned by 10, resulting in 15,000 posterior samples. Global convergence for the posterior samples was assessed via the Geweke diagnostic on the likelihood ($p > 0.05$); see Figure S2 of the supplementary materials for trace plots of log-likelihood and selected parameters. The analysis took approximately 8 hours on an M1 Macbook Pro with 8 gigabytes of memory.

5.2 Results

Overview Figure 4 illustrates the spatial heterogeneity of the tumor-immune interaction both within biopsies (captured by the standard deviation of sub-regional θ estimates) and between them (captured by the mean of the θ estimates). Biopsy level means ranged from -0.09 to 0.49, while biopsy level standard deviations ranged from 0.02 to 0.32. The absolute value of the coefficients of variation also ranged considerably, the minimum being 0.08 and the maximum being 437. This illustrates the degree to which the average level of interaction within a biopsy can vary separately from the level of heterogeneity within a biopsy.

The left panel of Figure 5 shows the relative magnitudes of the selected fixed and random effects, while the right panel shows the results of selection for fixed effects as well as random effects by immune cell sub-class. As described in Section 4, fixed effects and random effects were considered selection if their posterior probability of selection was greater than 0.5.

Ultimately, there were 35 covariates for which the fixed effect, random effect, or both were determined to be significant- see Table S3 of the supplementary materials for the full list along with immune cell group and effect selection. These genes came from 6 of the 7 total immune cell subtypes: macrophages, monocytes, neutrophils, natural killer cells, plasma cells, and T cells. The key results from the groups with selected genes are detailed in the following paragraphs.

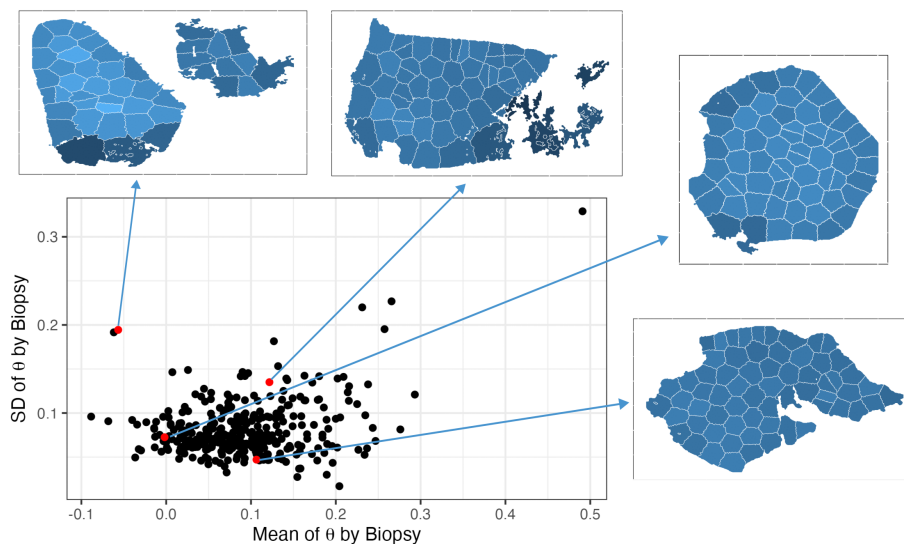


Figure 4: Distribution of spatial interactions within and across biopsies. Standard deviation of cellular spatial interaction parameter (θ) plotted against mean θ parameter at the biopsy level. Also shown are selected biopsy level plots of θ by sub-region (darker shades imply higher interaction) .

Neutrophils The immune cell group with the largest number of effects selected was the Neutrophil group. Neutrophils play a complex role in the tumor microenvironment, having been observed to have both pro- and anti-tumorigenic impacts depending on context (Powell and Huttenlocher 2016). Notably, one of the genes for which both the fixed effect and random effect was selected was PLXNC1, from the Neutrophil gene set. Increased expression of PLXNC1 was associated with increased tumor-immune interaction between biopsies. This is consistent with previous biological research that has suggested that PLXNC1 may act as a tumor suppressor, stymying progression and metastasis (Scott et al. 2009). The combined gene covariate Neutrophil_1 consisted of the genes S100A8 and S100A9, and was

negatively associated with interaction. This is highly consistent with previous results that indicate that expression of one or both of these genes is inversely associated with overall survival in melanoma patients (Pour et al. 2021). We thus find evidence in our results for the temperamental nature of neutrophil presence in the tumor microenvironment.

T cells While often treated as a monolith, the T cell family consists of many sub-types which play vastly differing roles in the TME. For example, while CD8+ T cells are widely regarded as a key part of the anti-tumorigenic immune response, regulatory T cells can actually have a pro-tumorigenic impact by suppressing immune response (Xie et al. 2021). The combined gene covariate T_1 consisted of 72 genes, the full list of which is available in Table S2 of the supplementary materials, and was positively associated with interaction. While interpretation is intrinsically more difficult due to the number of genes being combined, this set most notably contained the genes CD8A (often referred to as CD8) and CD3E (often referred to as CD3). The presence of one or both of these genes has been used as a proxy for the presence of cytotoxic lymphocytes in the context of multiplex imaging (Qin et al. 2022). It is thus unsurprising that their expression at the biopsy level would be associated with the presence of such cytotoxic cells, and thus increased interaction between immune cells and tumor cells. Finally, among the genes where the random effects were selected was IL23A. IL23A is a pro-inflammatory cytokine that has been shown to be associated with invasiveness in melanoma (Klein et al. 2015). While a number of different phenotypes could correspond to increased heterogeneity within a biopsy, it is intuitive that such heterogeneity would be associated with increased inflammation and invasiveness into the surrounding tissue.

Monocytes The role of monocytes in the tumor microenvironment is complex, primarily due to the fact that monocytes can differentiate into both macrophages and dendritic cells, each of which has different implications for patient prognosis. While tumor-associated macrophages are generally associated with poor patient prognosis, tumor-associated den-

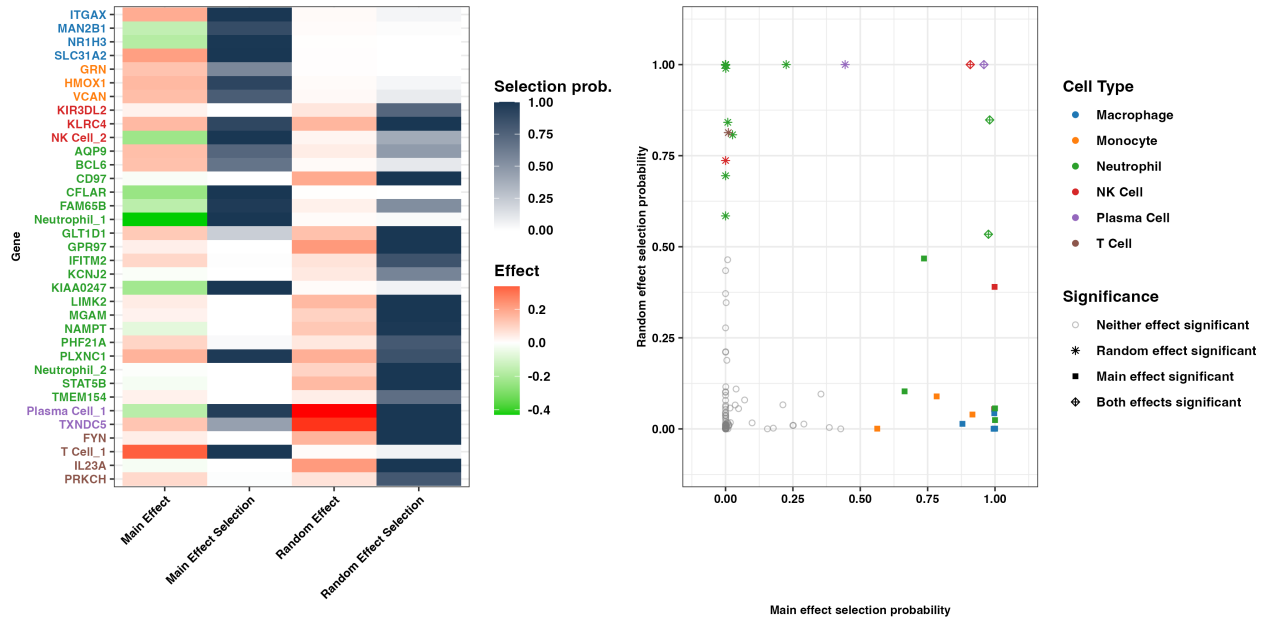


Figure 5: Left panel: heatmap of selection probabilities and effect magnitude for fixed and random effects for selected genes. Posterior mean and selection probabilities for main effects and random effects. Gene names are colored according to immune class membership. **Right panel: Selection results from gene expression analysis.** Posterior probability of random effect selection plotted against posterior probability of fixed effect selection. Color indicates class of immune cells the gene belongs to; shape indicates whether or not the effect was selected using the median-probability selection model described in Section 4.

drutic cells are generally associated with positive prognosis (Ugel et al. 2021). Amongst the selected genes in the monocyte group, two stood out based on their prior established importance in melanoma: HMOX1 and VCAN. HMOX1 has been shown to be genetically linked to risk of melanoma (Okamoto et al. 2006). Further, downregulating HMOX1 has been shown to be associated with increased interaction between natural killer cells and the tumor (Furfaro et al. 2020). This is somewhat incongruous with our result, since the estimated fixed effect term for HMOX1 is positive; however, since we are essentially adjusting for natural killer cell presence by proxy (i.e. expression of genes related to natural killer cells), such an association is not a priori biologically impossible. It has also been established that VCAN is overexpressed in melanoma relative to comparable healthy cells and that VCAN is associated with increased proliferation and in certain melanoma lineages (Touab 2002; Hernández 2011).

6 Discussion and limitations

In this paper, we propose a method called `DreameSpase` for integrative analyses of digital pathology imaging and genomics data. `DreameSpase` provides a novel spatially structured regression framework for joint modeling of high resolution spatial data from non-conformable spaces (i.e. biopsies) and associated (biopsy-level) covariates (i.e. gene expression data). This is accomplished by positing a structured regression model with covariate-specific spatial random effects which are modelled using CAR-based spatial processes. Furthermore, we induce sparsity by generalizing the traditional spike and slab priors used for fixed effect selection to the selection of spatial random that captures the intra-space heterogeneity. We demonstrate via simulation studies that the model reliably detects inter-space heterogeneity via the fixed effect selection mechanism, and intra-space heterogeneity via the random effect selection mechanism. Finally, we demonstrate the utility of `DreameSpase` in the analysis of whole slide pathology imaging data by applying it to a set of images of melanoma biopsies and associated transcriptomics data.

Advances in scale and extent of imaging technologies has led to proliferation of quantitative imaging data across many diseases, especially cancer. This has allowed a systematic collation of high-resolution spatial datasets – at scale – across many patients. These include newer technologies such as spatial multiplexed tissue imaging that generates high-resolution images to study the associations of cellular spatial relationships with tumor growth, metastasis, drug resistance, and patient survival ([Van Dam et al. 2022](#)). Our model engenders joint modeling of such non-conformable spatial data, as well as assessment of inter and intra-patient heterogeneity and its association with patient level covariates.

There remain areas of improvement for the model. In our formulation, the selection of the fixed effects is modeled independently of the selection of the random effects. This may be a reasonable assumption, but there may be circumstances in which it may be desirable

to allow for the modeling of a broader class of relationships between the selection of the two types of effects. Another shortcoming is the formulation of the random effect selection. The random effect selection suffers from a “piranha problem” whereby if too many null random effects are included in the model, it can be challenging for the model to properly select random effects. This is because each random effect, even if unselected, must have positive variance and thus account for some small part of the variance of the outcome. In practice, the estimated values of these random effects tend to be quite small individually, but large enough in aggregate that if too many are included, the ability of the model to select true random effects may suffer. In addition to these areas of improvement, there are also natural potential areas of extension. While we have limited our inquiry to genomic data, the model could naturally be extended in the future to multi-omic data (e.g. proteomic, metabolomic data). While other types of data could simply be included as covariates, it would perhaps be desirable to introduce group or more structured priors in such a setting ([Zhang et al. 2014](#)). Such priors could be used to select broad types of covariates (e.g. proteomics vs. genomics) but also potential pathways and families of genes. We leave these tasks for future exploration.

Software and data availability We have developed a general purpose software package that is available as a public Github repository. The package includes an efficient implementation of the Gibbs sampler algorithm discussed in this paper as well as methods to simulate data from the model. The sampling algorithm is implemented in C++ for improved efficiency. Data used in the analysis are provided in a separate Github repository with scripts to reproduce the analysis, tables and figures. This repository is modular in nature so that individual tables and figures can be reproduced as necessary.

References

- Abousamra, S., Gupta, R., Hou, L., Batiste, R., Zhao, T., Shankar, A., Rao, A., Chen, C., Samaras, D., Kurc, T., and Saltz, J. (2022). Deep learning-based mapping of tumor infiltrating lymphocytes in whole slide images of 23 types of cancer. *Frontiers in Oncology*, 11:806603.
- Barbieri, M. M. and Berger, J. O. (2004). Optimal predictive model selection. *The Annals of Statistics*, 32(3).
- Baxi, V., Edwards, R., Montalto, M., and Saha, S. (2022). Digital pathology and artificial intelligence in translational medicine and clinical practice. *Modern Pathology*, 35(1):23–32.
- Bowman, F. D. (2014). Brain imaging analysis. *Annual Review of Statistics and Its Application*, 1(1):61–85.
- Chervoneva, I., Peck, A. R., Yi, M., Freydin, B., and Rui, H. (2021). Quantification of spatial tumor heterogeneity in immunohistochemistry staining images. *Bioinformatics*, 37(10):1452–1460.
- Chesney, J., Puzanov, I., Collichio, F., Singh, P., Milhem, M. M., Glaspy, J., Hamid, O., Ross, M., Friedlander, P., Garbe, C., Logan, T. F., Hauschild, A., Lebbé, C., Chen, L., Kim, J. J., Gansert, J., Andtbacka, R. H., and Kaufman, H. L. (2018). Randomized, open-label phase ii study evaluating the efficacy and safety of talimogene laherparepvec in combination with ipilimumab versus ipilimumab alone in patients with advanced, unresectable melanoma. *Journal of Clinical Oncology*, 36(17):1658–1667.
- Clark, K., Vendt, B., Smith, K., Freymann, J., Kirby, J., Koppel, P., Moore, S., Phillips, S., Maffitt, D., Pringle, M., Tarbox, L., and Prior, F. (2013). The cancer imaging archive (tcia): Maintaining and operating a public information repository. *Journal of Digital Imaging*, 26(6):1045–1057.

- Falcone, I., Conciatori, F., Bazzichetto, C., Ferretti, G., Cognetti, F., Ciuffreda, L., and Milella, M. (2020). Tumor microenvironment: Implications in melanoma resistance to targeted therapy and immunotherapy. *Cancers*, 12(10):2870.
- Furfaro, A. L., Ottonello, S., Loi, G., Cossu, I., Piras, S., Spagnolo, F., Queirolo, P., Marinari, U. M., Moretta, L., Pronzato, M. A., Mingari, M. C., Pietra, G., and Nitti, M. (2020). Ho-1 downregulation favors brafv600 melanoma cell death induced by vemurafenib/plx4032 and increases nk recognition. *Int. J. Cancer*.
- George, E. I. and McCulloch, R. E. (1993). Variable selection via gibbs sampling. *Journal of the American Statistical Association*, 88(423):881–889.
- Goldman, M. J., Craft, B., Hastie, M., Repečka, K., McDade, F., Kamath, A., Banerjee, A., Luo, Y., Rogers, D., Brooks, A. N., et al. (2020). Visualizing and interpreting cancer genomics data via the xena platform. *Nature biotechnology*, 38(6):675–678.
- Hanahan, D. (2022). Hallmarks of cancer: New dimensions. *Cancer Discovery*, 12(1):31–46.
- Heindl, A., Nawaz, S., and Yuan, Y. (2015). Mapping spatial heterogeneity in the tumor microenvironment: a new era for digital pathology. *Laboratory Investigation*, 95(4):377–384.
- Hernández, D. (2011). V3 versican isoform alters the behavior of human melanoma cells by interfering with cd44/erbB-dependent signaling. *Journal of Biological Chemistry*, 286(2).
- Huijben, I. A. M., Kool, W., Paulus, M. B., and Van Sloun, R. J. G. (2023). A review of the gumbel-max trick and its extensions for discrete stochasticity in machine learning. *IEEE Transactions on Pattern Analysis and Machine Intelligence*, 45(2).
- Högmander, H. and Särkkä, A. (1999). Multitype spatial point patterns with hierarchical interactions. *Biometrics*, 55(4):1051–1058.
- Ibrahim, J. G., Zhu, H., Garcia, R. I., and Guo, R. (2011). Fixed and random effects selection in mixed effects models. *Biometrics*, 67(2):495–503.
- Joyner, C. N., McMahan, C. S., Tebbs, J. M., and Bilder, C. R. (2020). From mixed effects modeling to spike and slab variable selection: A bayesian regression model for group

- testing data. *Biometrics*, 76(3):913–923.
- Kang, K., Xie, F., Mao, J., Bai, Y., and Wang, X. (2020). Significance of tumor mutation burden in immune infiltration and prognosis in cutaneous melanoma. *Frontiers in Oncology*, 10:573141.
- Klein, A., Schwartz, H., Sagi-Assif, O., Meshel, T., Izraely, S., Ben Menachem, S., Bengaiev, R., Ben-Shmuel, A., Nahmias, C., Couraud, P.-O., et al. (2015). Astrocytes facilitate melanoma brain metastasis via secretion of il-23. *The Journal of pathology*, 236(1):116–127.
- Krishnan, S. N., Mohammed, S., Frankel, T. L., and Rao, A. (2022). Gawrdenmap: a quantitative framework to study the local variation in cell–cell interactions in pancreatic disease subtypes. *Scientific Reports*, 12(1):3708.
- Li, Q., Wang, X., Liang, F., and Xiao, G. (2019a). A bayesian mark interaction model for analysis of tumor pathology images. *The Annals of Applied Statistics*, 13(3).
- Li, Q., Wang, X., Liang, F., Yi, F., Xie, Y., Gazdar, A., and Xiao, G. (2019b). A bayesian hidden potts mixture model for analyzing lung cancer pathology images. *Biostatistics*, 20(4):565–581.
- Li, X., Yang, Y., Huang, Q., Deng, Y., Guo, F., Wang, G., and Liu, M. (2021). Crosstalk between the tumor microenvironment and cancer cells: A promising predictive biomarker for immune checkpoint inhibitors. *Frontiers in Cell and Developmental Biology*, 9:738373.
- MacNab, Y. C. (2022). Bayesian disease mapping: Past, present, and future. *Spatial Statistics*, 50:100593.
- Marzagalli, M., Ebelt, N. D., and Manuel, E. R. (2019). Unraveling the crosstalk between melanoma and immune cells in the tumor microenvironment. *Seminars in Cancer Biology*, 59:236–250.
- Ni, Y., Stingo, F. C., and Baladandayuthapani, V. (2019). Bayesian graphical regression. *Journal of the American Statistical Association*, 114(525):184–197.

- Nirmal, A. J., Regan, T., Shih, B. B., Hume, D. A., Sims, A. H., and Freeman, T. C. (2018). Immune cell gene signatures for profiling the microenvironment of solid tumors. *Cancer Immunology Research*, 6(11):1388–1400.
- Okamoto, I., Kr, J., Mannhalter, C., Wagner, O., and Pehamberger, H. (2006). A microsatellite polymorphism in the heme oxygenase-1 gene promoter is associated with risk for melanoma. *International Journal of Cancer*.
- Orozco-Acosta, E., Adin, A., and Ugarte, M. D. (2022). Big problems in spatio-temporal disease mapping: methods and software. *Computer Methods and Programs in Biomedicine*, 231([arXiv:2201.08323](https://arxiv.org/abs/2201.08323)). [arXiv:2201.08323](https://arxiv.org/abs/2201.08323) [stat].
- Osher, N., Kang, J., Krishnan, S., Rao, A., and Baladandayuthapani, V. (2023). SpartIn: a bayesian method for the quantification and characterization of cell type interactions in spatial pathology data. *Frontiers in Genetics*.
- Pour, S. R., de Coaña, Y. P., Demorentin, X. M., Melief, J., Thimma, M., Wolodarski, M., Gomez-Cabrero, D., Hansson, J., Kiessling, R., and Tegner, J. (2021). Predicting anti-pd-1 responders in malignant melanoma from the frequency of s100a9+ monocytes in the blood. *Journal for immunotherapy of cancer*, 9(5).
- Powell, D. R. and Huttenlocher, A. (2016). Neutrophils in the tumor microenvironment. *Trends in Immunology*, 37(1):41–52.
- Qin, A., Lima, F., Bell, S., Kalemkerian, G. P., Schneider, B. J., Ramnath, N., Lew, M., Krishnan, S., Mohammed, S., Rao, A., and Frankel, T. L. (2022). Cellular engagement and interaction in the tumor microenvironment predict non-response to pd-1/pd-l1 inhibitors in metastatic non-small cell lung cancer. *Scientific Reports*, 12(1):9054.
- Sadeghi Rad, H., Monkman, J., Warkiani, M. E., Ladwa, R., O’Byrne, K., Rezaei, N., and Kulasinghe, A. (2021). Understanding the tumor microenvironment for effective immunotherapy. *Medicinal Research Reviews*, 41(3):1474–1498.
- Saltz, J., Gupta, R., Hou, L., Kurc, T., Singh, P., Nguyen, V., Samaras, D., Shroyer, K. R.,

- Zhao, T., Batiste, R., et al. (2018). Spatial organization and molecular correlation of tumor-infiltrating lymphocytes using deep learning on pathology images. *Cell reports*, 23(1):181–193.
- Scheipl, F., Fahrmeir, L., and Kneib, T. (2012). Spike-and-slab priors for function selection in structured additive regression models. *Journal of the American Statistical Association*, 107(500):1518–1532.
- Scott, G. A., McClelland, L. A., Fricke, A. F., and Fender, A. (2009). Plexin c1, a receptor for semaphorin 7a, inactivates cofilin and is a potential tumor suppressor for melanoma progression. *Journal of Investigative Dermatology*, 129(4):954–963.
- Simiczyjew, A., Dratkiewicz, E., Mazurkiewicz, J., Ziętek, M., Matkowski, R., and Nowak, D. (2020). The influence of tumor microenvironment on immune escape of melanoma. *International Journal of Molecular Sciences*, 21(21):8359.
- Sun, Y. (2016). Tumor microenvironment and cancer therapy resistance. *Cancer Letters*, 380(1):205–215.
- Touab, M. (2002). Versican is differentially expressed in human melanoma and may play a role in tumor development. *The American Journal of Pathology*, 160(2).
- Ugel, S., Canè, S., De Sanctis, F., and Bronte, V. (2021). Monocytes in the tumor microenvironment. *Annual Review of Pathology: Mechanisms of Disease*, 16(1):93–122.
- Van Dam, S., Baars, M. J. D., and Vercoulen, Y. (2022). Multiplex Tissue Imaging: Spatial Revelations in the Tumor Microenvironment. *Cancers*, 14(13):3170.
- Vu, T., Wrobel, J., Bitler, B. G., Schenk, E. L., Jordan, K. R., and Ghosh, D. (2022). Spf: A spatial and functional data analytic approach to cell imaging data. *PLOS Computational Biology*, 18(6):e1009486.
- Weinstein, J. N., Collisson, E. A., Mills, G. B., Shaw, K. R. M., Ozenberger, B. A., Ellrott, K., Shmulevich, I., Sander, C., and Stuart, J. M. (2013). The cancer genome atlas pan-cancer analysis project. *Nature Genetics*, 45(10):1113–1120.

- Xiao, X., Guo, Q., Cui, C., Lin, Y., Zhang, L., Ding, X., Li, Q., Wang, M., Yang, W., Kong, Y., and Yu, R. (2022). Multiplexed imaging mass cytometry reveals distinct tumor-immune microenvironments linked to immunotherapy responses in melanoma. *Communications Medicine*, 2(1):131.
- Xie, Q., Ding, J., and Chen, Y. (2021). Role of cd8+ t lymphocyte cells: Interplay with stromal cells in tumor microenvironment. *Acta Pharmaceutica Sinica B*, 11(6):1365–1378.
- Yang, H., Baladandayuthapani, V., and Morris, J. S. (2017). Quantile functional regression using quantlets. [arXiv:1711.00031 \[stat\]](https://arxiv.org/abs/1711.00031). arXiv: 1711.00031.
- Zhang, L., Baladandayuthapani, V., Mallick, B. K., Manyam, G. C., Thompson, P. A., Bondy, M. L., and Do, K.-A. (2014). Bayesian hierarchical structured variable selection methods with application to molecular inversion probe studies in breast cancer. *Journal of the Royal Statistical Society Series C: Applied Statistics*, 63(4):595–620.
- Zoghi, S., Masoumi, F., and Rezaei, N. (2023). The immune system. In *Clinical Immunology*, pages 1–46. Elsevier.

Spatially Structured Regression for Non-conformable Spaces: Integrating Pathology Imaging and Genomics Data Supplementary Materials

June 25, 2024

Contents

S1	Pre-Processing	1
	S1.1 H&E Data	1
	S1.2 Hierarchical Strauss Model Fitting	1
	S1.3 Posterior Distributions of θ	2
S2	Simulation	3
	S2.1 Signal to Noise Ratio	3
	S2.1.1 Fixed Effect Signal to Noise Ratio	3
	S2.1.2 Random Effect Signal to Noise Ratio	3
	S2.2 Additional Simulation Results	3
S3	Application	4
	S3.1 Gumbel Max Trick Derivation	4
	S3.2 Gene Expression Pre-Processing	5
	S3.3 Full Conditional Distributions	5
	S3.3.1 Main Effect Group	7
	S3.3.2 Random Effect Group	7
	S3.3.3 Error terms	8
	S3.4 Selected Genes	9
	S3.5 Model Trace Plots	10

arXiv:2406.16721v1 [stat.AP] 24 Jun 2024

S1 Pre-Processing

S1.1 H&E Data

335 high definition images were obtained from The Cancer Genome Atlas Genomic Data Commons Data Portal. 20 images were used to train a cell classification model. A total of 1,250 cells were annotated by a pathologist. These annotated cells were subsequently used to train a random forest model to classify the types of cells in each image as Tumor, Immune, Macrophage, or Other based on morphology characteristics of the cell nuclei. The classifier achieved an accuracy in the range of 87%-91%. In addition to the type of each cell, the x- and y- coordinates of the centroid of each cell were determined. This process therefore yielded three pieces of information for each cell in the biopsy: the type, the x-coordinate, and the y-coordinate. For more details on the classifier and pre-processing, see Osher et al. 2023.

S1.2 Hierarchical Strauss Model Fitting

Model fitting for the Hierarchical Strauss Model (HSM) is based on the Pseudolikelihood function, which is itself based on the Papangelou conditional intensity function. Let $\Theta = [\beta_1, \beta_2, \theta]^T$ be the parameters of the

HSM, $x = [x_1^T, x_2^T]^T$ be the observed points, and let the density $f(x; \Theta)$ be the likelihood evaluated on a given point pattern x for a set of parameters Θ . Then the Papangelou conditional intensity at a point u is defined by:

$$\lambda(u|\Theta, x) = \begin{cases} \frac{f(x \cup \{u\}; \Theta)}{f(x; \Theta)} & u \notin x \\ \frac{f(x; \Theta)}{f(x - \{u\}; \Theta)} & u \in x \end{cases} \quad (\text{S1})$$

The pseudolikelihood (PL) is in turn defined based on the Papangelou conditional intensity. Because the PL involves an integral, a quadrature based approximation is often used in place of the PL function (and in turn the log-PL function). A u is selected, with corresponding weights w . The pseudolikelihood function can then be defined as follows:

$$PL(\Theta|x) \approx \prod_{x_i \in x} \lambda(x_i|\Theta, x) \exp\left(-\sum_{u_j \in u} \lambda(u_j|\Theta, x)w_j\right) \quad (\text{S2})$$

Yielding a log-PL function of:

$$\log PL(\Theta|x) \approx \sum_{x_i \in x} \log(\lambda(x_i|\Theta, x)) - \sum_{u_j \in u} \lambda(u_j|\Theta, x)w_j \quad (\text{S3})$$

The log-PL function is used as the target log-likelihood function, and traditional sampling methods can be used. We utilized the STAN statistical software to perform the posterior sampling of the Θ parameter.

S1.3 Posterior Distributions of θ

Figure S1 shows examples of posterior distributions for the θ parameter for various sub-regions of various biopsies. These posteriors tend to be relatively Gaussian.

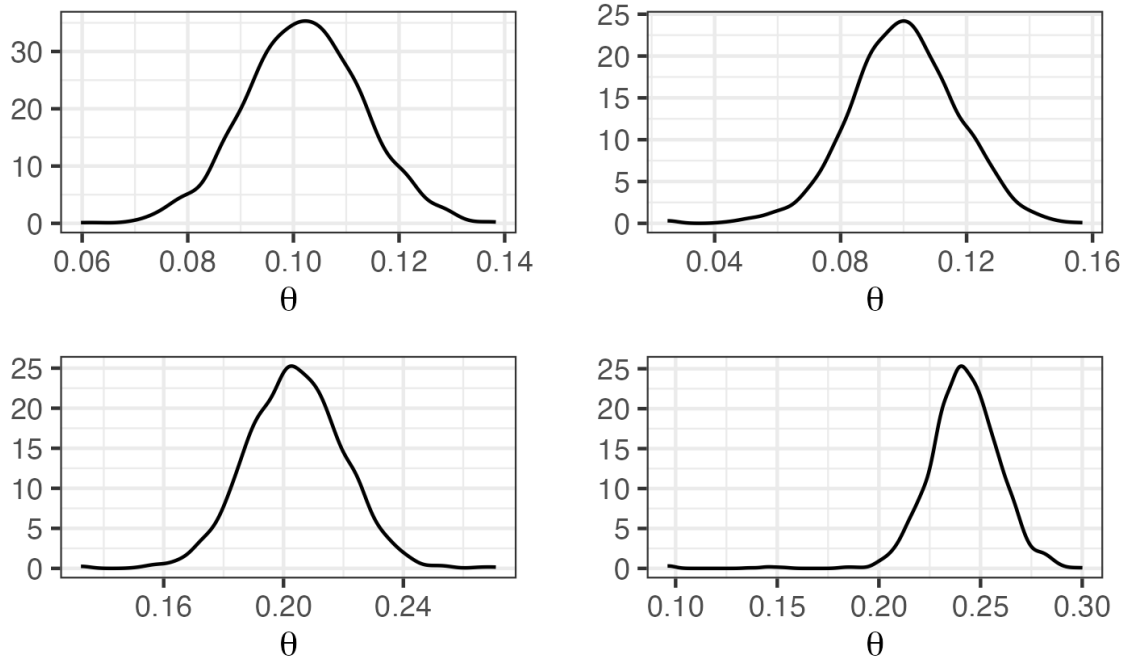


Figure S1: **Posterior distributions of θ .** Example posterior distributions of θ parameter for various sub-regions of biopsies in the data set.

S2 Simulation

S2.1 Signal to Noise Ratio

S2.1.1 Fixed Effect Signal to Noise Ratio

Let us assume that the covariates follow some distribution with covariance matrix Σ_x and mean $\mu_x = [\mu_1, \dots, \mu_p]^T$. Then denoting the marginal variance of the outcome Y across all biopsies by $\text{var}(Y)$:

$$SNR_{fixed} = \frac{\text{var}(X^T \alpha)}{\text{var}(Y)} \quad (\text{S4})$$

This can be thought of as an R^2 value, in that it represents the proportion of variance explained by the fixed effects. When α is treated as a fixed constant, by basic properties of covariance we have $\text{var}(X^T \alpha) = \alpha^T \Sigma_x \alpha$. Because this value depends only on the joint distribution of the covariates, the values of the fixed effects, and the marginal distribution of the outcome, it is common across all biopsies.

S2.1.2 Random Effect Signal to Noise Ratio

The signal to noise ratio for the random effects is defined analogously to those of the fixed effects. However, the signal to noise ratio must be considered at the level of a given biopsy rather than across all biopsies. This is because of the assumptions of the CAR model: biopsies with adjacency structures such that sub-regions tend to have fewer neighbors will have greater variance associated with the spatial random effects, and vice versa for adjacency structures such that sub-regions tend to have more neighbors. Note that this also means that within a biopsy, the level of variance attributable to the spatial random effect for a given sub-region will depend on the number of neighbors that sub-region has.

Dropping patient index i for ease of notation, let $\eta_{j\cdot}$ denote the j th row of $\eta_i(S_i)$. Then define the mean SNR for a biopsy with adjacency matrix W and n sub-regions by:

$$SNR_{rand} = \frac{\sum_{j=1}^n \text{var}(\eta_{j\cdot}, X)}{n \text{var}(Y)} \quad (\text{S5})$$

In other words, the signal to noise for the random effect component for a given biopsy is the ratio of the average variance accounted for by the random effect across the sub-regions. Note that because the variance of the outcome for a given biopsy may be larger than that of the marginal variance of the outcome, this term cannot be interpreted as a proportion of variance explained in the same manner as the fixed effect SNR, since it can be larger than one.

Because both $\eta_{j\cdot}$ and X are being treated as random quantities, the term $\text{var}(\eta_{j\cdot}, X)$ requires modestly more thought. Because the entries of $\eta_{j\cdot}$ are independent, it is easiest to think of this as $\text{var}(\sum_{k=1}^p \eta_{jk} X_k)$, which by the law of total variance and the independence of the entries of $\eta_{j\cdot}$ is equal to

$$\begin{aligned} & \text{var} \left(E \left[\sum_{k=1}^p \eta_{jk} X_k \mid \eta_{j\cdot} \right] \right) + E \left[\text{var} \left(\sum_{k=1}^p \eta_{jk} X_k \mid \eta_{j\cdot} \right) \right] \\ &= \text{var} \left(\sum_{k=1}^p \eta_{jk} \mu_k \right) + E \left[\eta_{j\cdot} \Sigma_x \eta_{j\cdot}^T \right] \\ &= \sum_{k=1}^p \mu_k^2 \text{var}(\eta_{jk}) + \sum_{k=1}^p E[\eta_{jk}^2] \sigma_k^2 \end{aligned}$$

Where σ_k^2 is the k th diagonal entry of Σ_x . Because $E[\eta_{j\cdot}] = 0$, this reduces to

$$= \sum_{k=1}^p \text{var}(\eta_{jk})(\mu_k^2 + \sigma_k^2)$$

Here again $\text{var}(\eta_{jk})$ refers to the variance of the j th covariate specific CAR random effect for the k th covariate, which is the j th entry of $\psi_k^2 [D_w(W) - \phi W]^{-1}$; again this cannot be written more simply.

Finally, note that by definition $\text{var}(\varepsilon_i) = \nu^2$.

S2.2 Additional Simulation Results

Define AUC_p as the area under the ROC curve limited to false positive rate p . This means that rather than lying between 0 and 1 like standard AUC , AUC_p will lie between 0 and p . Table S1 shows the $AUC_{0.1}$ and

Table S1: $AUC_{0.1}$ and $AUC_{0.2}$ for simulations. $AUC_{0.1}$ refers to the AUC computed such that the maximal FPR considered is 0.1, with $AUC_{0.2}$ defined analogously. Thus, $AUC_{0.1} \in [0, 0.1]$, and $AUC_{0.2} \in [0, 0.2]$. For the purposes of the tables below, both have been multiplied by 10 and 5, respectively, to put them in the same range of AUC (between 0.5 and 1). The “analyst model” performs quite well for random effect selection, but notably less well for fixed effect selection. The *DreamSpace* model performs marginally worse than the “analyst model” in Random Effect selection in the latter two settings, but considerably better in the fixed effect setting.

AUC_{0.1}	Main Effects			Random Effects		
$\frac{2p}{n}$	“Analyst Model”	NSDS	<i>DreamSpace</i>	“Analyst Model”	NSDS	<i>DreamSpace</i>
0.5	0.47	1	1	0.99	0.99	0.99
0.75	0.51	1	1	0.97	0.82	0.94
0.9	0.51	1	1	0.92	0.65	0.81

AUC_{0.2}	Main Effects			Random Effects		
$\frac{2p}{n}$	“Analyst Model”	NSDS	<i>DreamSpace</i>	“Analyst Model”	NSDS	<i>DreamSpace</i>
0.5	0.47	1	1	1	0.99	0.99
0.75	0.51	1	1	0.98	0.84	0.96
0.9	0.51	1	1	0.95	0.7	0.84

$AUC_{0.2}$ for the three models. In order to compute AUC_p , the TPR/FPR pair for $FPR = p$ was estimated by linearly interpolating the observed pair with the largest FPR less than p and the observed pair with the smallest FPR greater than p . For example, if we observe an FPR/TPR pair of 0.19, 0.49 and 0.21, 0.51, we would estimate that $TPR = 0.52$ when $FPR = 0.2$. The area under the curve is computed empirically, i.e. treating the observed pairs as a step function and integrating it.

S3 Application

S3.1 Gumbel Max Trick Derivation

Suppose $\gamma_1, \dots, \gamma_k$ are log non-normalized probabilities of a categorical distribution; we will treat these values as fixed. Let $G(\mu)$ denote the Gumbel distribution with scale parameter 1 and location parameter μ . Denote the CDF of each distribution by $F_\mu(x) = \exp(-\exp(-(x - \mu)))$ and the PDF by $f_\mu(x) = \exp(-(x - \mu) - \exp(-(x - \mu)))$. Let g_1, \dots, g_k be samples with $g_j \sim G(\gamma_j)$. Consider the probability that g_j is the largest among all g_1, \dots, g_k . Conditional upon the value of g_j , the probability that g_j is the largest is simply

$$\begin{aligned}
 P(g_1, \dots, g_{j-1}, g_{j+1}, \dots, g_k < g_j | g_j) &= \prod_{i \neq j} P(g_i < g_j) \\
 &= \prod_{i \neq j} F_{\gamma_i}(g_j) \\
 &= \prod_{i \neq j} \exp(-\exp(-(g_j - \gamma_i))) = \exp(-\exp(-g_j) \sum_{i \neq j} \exp(\gamma_i))
 \end{aligned} \tag{S6}$$

Thus,

$$\begin{aligned}
P(g_1, \dots, g_{j-1}, g_{j+1}, \dots, g_k < g_j) &= E[I(g_1, \dots, g_{j-1}, g_{j+1}, \dots, g_k < g_j)] \\
&= E_{g_j}[E[I(g_1, \dots, g_{j-1}, g_{j+1}, \dots, g_k < g_j)|g_j]] \\
&= E_{g_j}[\exp(-\exp(-g_j) \sum_{i \neq j} \exp(\gamma_i))] \\
&= \int_{-\infty}^{\infty} \exp(-\exp(-g_j) \sum_{i \neq j} \exp(\gamma_i)) \exp(-(g_j - \gamma_j) - \exp(-(g_j - \gamma_j))) dg_j \quad (S7) \\
&= \int_{-\infty}^{\infty} \exp(-(g_j - \gamma_j) - \exp(-g_j) \sum_{i=1}^k \exp(\gamma_i)) dg_j \\
&= \frac{\exp(\gamma_j)}{\sum_{i=1}^k \exp(\gamma_i)} \exp(-\exp(-g_j) \sum_{i=1}^k \exp(\gamma_i)) \Big|_{-\infty}^{\infty} = \frac{\exp(\gamma_j)}{\sum_{i=1}^k \exp(\gamma_i)}
\end{aligned}$$

Which is precisely the marginal probability of drawing from category j in the categorical distribution.

S3.2 Gene Expression Pre-Processing

The pre-processing of the gene expression data used in the application analysis proceeded as follows. Within the seven groups of genes, the pairwise correlation was computed between all pairs of genes. Genes were then gathered into sets such that for all genes in a given group, there was at least one other gene in that set for which the pairwise correlation was at least 0.8. Note that such sets would consist of a single gene if a given gene was not highly correlated with any other genes. The expression of all genes within a given group were then averaged to yield a single value, which was ultimately used in the analysis.

Equivalently, this process can be thought of as forming a graph within each group where each gene represents a vertex, and there is an edge between two vertices (genes) if their pairwise correlation is greater than 0.8. Each subgroup represents a disjoint sub-graph of the resulting graph. This process is described in the Algorithm S1. This process resulted in 9 sets with more than one gene. The sets and the genes they contain are shown in Table S2.

Algorithm S1 Gene Expression Pre-Processing

```

for  $G_i$  in {Gene group 1, ..., Gene group 7} do
  for  $k = 1 \dots N_{G_i}$  do  $\triangleright N_{G_i}$  is the number of genes in group  $G_i$ 
    if  $g_{ik}$  is not currently in a set then
      create a new set,  $C_{ik} = \{g_{ik}\}$ 
    end if
    for  $j = i + 1 \dots N_{G_i}$  do
      if  $Cor(g_{ij}, g_{ik}) > 0.8$  then
        merge sets of  $g_{ij}, g_{ik}$ 
      end if
    end for
  end for
end for
for  $C_{\ell m}$  in  $C_{11}, \dots, C_{1N_{C_1}}, \dots, C_{71}, \dots, C_{7N_{C_7}}$  do  $\triangleright N_{C_i}$  is the number of sets for group  $i$ 
  compute  $E_{\ell m} = \frac{1}{|C_{\ell m}|} \sum_{t=1}^{|C_{\ell m}|} g_t$ 
end for
return  $E_{11}, \dots, E_{1N_{C_1}}, \dots, E_{71}, \dots, E_{7N_{C_7}}$ 

```

S3.3 Full Conditional Distributions

This section outlines the derivations of the full conditional distributions for all parameters in the model. The derivation is divided into three parts: one for the main effects and associated terms, one for the random effects and associated terms, and one for the error terms.

Table S2: **Gene sets and component genes.** Each gene set consists of two or more gene, with all genes in the group having a correlation between their expression of at least 0.8. The average expression of each set is included in the model as a single covariate.

Gene set	Genes
B_1	BANK1; HLA-DOB; CD72; TLR10; CD19; TCL1A; MS4A1; STAP1; BTLA; CR2; FCRL2; CD180; VPREB3; FCRL1; FCRL3; FAM129C; FCRL5; CD79A; CCR6; LY9; CD37; KIAA0125; PNOC; PAX5; POU2F2; S1PR4; BLK
Macrophage_1	CECR1; SLAMF8; IFI30; CCR1; CD163; ITGB2; C1QB; C3AR1; FCER1G; TYROBP; TNFAIP2; SLC15A3; CD74; CLEC7A; NCKAP1L; SPI1; CYBB; VSIG4; HK3; IGSF6; MSR1; LILRB4; CD300A; TLR8; MNDA; FCGR1B; FPR3; FCGR1A; CD4; MYO1F; CYTH4; CD86; LAIR1; LAPTM5; ADAMDEC1; CMKLR1; MS4A7; TNFRSF1B; MS4A4A; CTSS; AOH; ITGAM; CSF1R; C1QA; C5AR1; ATP8B4; CCRL2; SLCO2B1
Neutrophil_1	FPR1; CSF3R; LILRA2; NCF4
T_1	GIMAP4; CD2; ARHGAP9; CD48; RASSF5; CD52; ARHGAP25; TBC1D10C; NLRC3; C1orf162; SP140; GPR18; HCST; RHOH; GZMK; CORO1A; ITGAL; GIMAP7; TRAF3IP3; EVI2B; DOCK2; IL10RA; LCP1; CD27; FAM26F; DOCK8; CD3G; GIMAP2; NCF1B; FLI1; CXCR6; SH2D1A; PVRIG; CYTIP; TRAT1; CD3E; GIMAP6; CD96; CD3D; CRTAM; CCL19; BIN2; PARVG; TARP; KLRB1; CCR7; CD6; UBASH3A; PSTPIP1; IL7R; GPR171; APBB1IP; AMICA1; BTK; PTPRCAP; ITK; SLA; GIMAP5; RCSD1; SASH3; TNFRSF9; CD28; HVCN1; CXCL9; LY86; RGS18; DPEP2; SIRPG; CD8A; ICOS; GAB3; GMFG
NK_1	KLRC3; KLRC2
Monocyte_1	PILRA; LILRB2; HCK; LILRB3; LST1; AIF1; LILRA6; CD300LF; FGR; CD14; C10orf54; SLC7A7; NFAM1; PRAM1; LRRC25
Neutrophil_2	S100A9; S100A8
NK_2	TBX21; KIR2DL4; PRF1; SAMD3; KLRD1
Plasma_1	TNFRSF17; IGJ

S3.3.1 Main Effect Group

Main Effects We begin by defining the following quantities:

$\mathbf{Y}_{i,\alpha}^* = \mathbf{Y}_i - \boldsymbol{\eta}_i \mathbf{X}_i - \boldsymbol{\delta}_i(\mathbf{S}_i)$, $\bar{Y}_{i,\alpha}^* = \frac{1}{n_i}(1^T \mathbf{Y}_{i,\alpha}^*)$ (i.e. the mean of each $Y_{i,\alpha}^*$), and $\bar{\mathbf{Y}}_\alpha^* = [\bar{Y}_{1,\alpha}^*, \dots, \bar{Y}_{N,\alpha}^*]^T$. Note that $\pi(\bar{Y}_{i,\alpha}^* | \cdot) \sim N(\boldsymbol{\alpha}^T \mathbf{X}_i, \frac{\nu^2}{n_i^2})$.

Further, defining the $N \times p$ matrix \mathbf{X} such that $[\mathbf{X}]_{ij} = X_{ij}$, i.e. the j th covariate of the i th patient, then trivially we have $\pi(\boldsymbol{\alpha} | \cdot) \propto \pi(\bar{\mathbf{Y}}_\alpha^* | \boldsymbol{\alpha}, \nu^2) \pi(\boldsymbol{\alpha} | \gamma_1, \dots, \gamma_p, \sigma_{spike}^2, \sigma_{slab}^2)$. Denoting $\boldsymbol{\Gamma} = \text{diag}(\gamma_1 \cdot \sigma_{slab}^2 + (1 - \gamma_1) \cdot \sigma_{spike}^2, \dots, \gamma_p \cdot \sigma_{slab}^2 + (1 - \gamma_p) \cdot \sigma_{spike}^2)$, i.e. the prior covariance of $\boldsymbol{\alpha}$ conditional on $\gamma_1, \dots, \gamma_p$, and denoting $\mathbf{D} = \text{diag}(\frac{\nu^2}{n_1^2}, \dots, \frac{\nu^2}{n_p^2})$ the full conditional for $\boldsymbol{\alpha}$ is

$$\pi(\boldsymbol{\alpha} | \cdot) = \text{MVN}((\boldsymbol{\Gamma}^{-1} + \nu^{-2} \mathbf{X}^T \mathbf{D}^{-1} \mathbf{X})^{-1} \mathbf{X}^T \mathbf{D}^{-1} \bar{\mathbf{Y}}_\alpha^*, (\boldsymbol{\Gamma}^{-1} + \nu^{-2} \mathbf{X}^T \mathbf{D}^{-1} \mathbf{X})^{-1})$$

This is simply the standard full conditional distribution for the main effects of a linear regression with an informative prior and heteroschedastic error variance.

Main Effect Selection Indicators For each main effect selection indicator γ_j , $j = 1, \dots, p$, by definition γ_j takes on the value either 0 or 1. Thus, given the prior $P(\gamma = 1) = p_{\gamma,1}$ and $P(\gamma = 0) = p_{\gamma,0}$, it follows that $P(\gamma_j = k | \cdot) \propto \pi(\alpha_j | \gamma, \cdot) p_{\gamma,k}$ for $k = 0, 1$. Defining $\sigma_k^2 = k\sigma_{slab}^2 + (1 - k)\sigma_{spike}^2$, this implies that the full conditional for γ_j is given by:

$$P(\gamma = k | \cdot) = \frac{\frac{1}{\sqrt{2\pi\sigma_k^2}} \exp\left(\frac{-1}{2\sigma_k^2} \alpha_j^2\right) p_{\gamma,k}}{\frac{1}{\sqrt{2\pi\sigma_{spike}^2}} \exp\left(\frac{-1}{2\sigma_{spike}^2} \alpha_j^2\right) p_{\gamma,0} + \frac{1}{\sqrt{2\pi\sigma_{slab}^2}} \exp\left(\frac{-1}{2\sigma_{slab}^2} \alpha_j^2\right) p_{\gamma,1}}$$

Main Effect Selection Probability The final term in the main effect group is the main effect selection probability term, P_γ . This term captures the proportion of main effects selected. The combination of the uninformative beta prior in P_γ and the binary $\gamma_1, \dots, \gamma_p$, the full conditional of P_γ trivially reduces to that of a standard beta-binomial model:

$$\pi(P_\gamma | \cdot) = \text{Beta}\left(1 + \sum_{j=1}^p \gamma_j, 1 + \left[p - \sum_{j=1}^p \gamma_j\right]\right)$$

S3.3.2 Random Effect Group

Spatial Random Effects The full conditional of ψ_j^2 is induced via the prior on ψ_j , and requires somewhat more careful derivation. We begin by noting that $\pi(\psi_j | \cdot) \propto \left[\prod_{i=1}^N \pi(\boldsymbol{\eta}_{i(j)}(\mathbf{S}_i) | \psi_j, \cdot)\right] \pi(\psi_j | d_j, \xi_{spike}^2, \xi_{slab}^2)$. More precisely, defining $\xi_k^2 = k\xi_{slab}^2 + (1 - k)\xi_{spike}^2$ this yields the full conditional kernel of:

$$\begin{aligned} \pi(\psi_j | d_j = k, \cdot) &\propto \prod_{i=1}^N \left[\det\left(\frac{1}{\psi_j^2} [D_w(\mathbf{W}_i) - \phi \mathbf{W}_i]\right)^{-1/2} \right. \\ &\quad \left. \exp\left(-\frac{1}{2} \left\{ \boldsymbol{\eta}_{i(j)}(\mathbf{S}_i)^T \left[\frac{1}{\psi_j^2} [D_w(\mathbf{W}_i) - \phi \mathbf{W}_i] \right]^{-1} \boldsymbol{\eta}_{i(j)}(\mathbf{S}_i) \right\}\right) \right] \\ &\quad \exp\left(\frac{-1}{2\xi_k^2} \psi_j^2\right) \end{aligned} \quad (\text{S8})$$

Let us denote $S = \sum_{i=1}^N n_i$, i.e. the total number of sub-regions across all biopsies. Using properties of the determinant and standard algebraic manipulation, equation 7 can be simplified to

$$\pi(\psi_j | d_j = k, \cdot) \propto (\psi_j)^{-S} \exp\left(-\frac{1}{2} \left[\sum_{i=1}^N \boldsymbol{\eta}_{i(j)}(\mathbf{S}_i)^T [D_w(\mathbf{W}_i) - \phi \mathbf{W}_i] \boldsymbol{\eta}_{i(j)}(\mathbf{S}_i) \right] \frac{1}{\psi_j^2} - \frac{1}{2\xi_k^2} \psi_j^2\right) \quad (\text{S9})$$

While it appears unusual at first glance, the right hand side of equation 8 is the kernel of a *Generalized Inverse Gaussian* distribution, parameterized, the kernel of which is given by:

$$f(x | a, b, c) \propto x^{c-1} \exp\left(-\frac{1}{2}\left(ax + \frac{b}{x}\right)\right)$$

However, this is with respect to ψ_j^2 , while the density itself is of ψ_j . Fortunately, because the variance ψ_j^2 is a monotonic transformation of the standard deviation ψ_j , it follows from this that the distribution of ψ_j^2 is given by

$$\begin{aligned} \pi(\psi_j^2 | d_j = k, \cdot) &\propto ((\psi_j^2)^{1/2})^{-S} \left| \frac{1}{2}(\psi_j^2)^{-1/2} \right| \\ &\exp\left(-\frac{1}{2} \left[\sum_{i=1}^N \boldsymbol{\eta}_{i(j)}(S_i)^T [D_w(W_i) - \phi W_i] \boldsymbol{\eta}_{i(j)}(S_i) \right] \frac{1}{((\psi_j^2)^{1/2})^2} - \frac{1}{2\xi_k^2} ((\psi_j^2)^{1/2})^2 \right) \\ &= (\psi_j^2)^{-(S+1)/2} \exp\left(-\frac{1}{2} \left\{ \left[\sum_{i=1}^N \boldsymbol{\eta}_{i(j)}(S_i)^T [D_w(W_i) - \phi W_i] \boldsymbol{\eta}_{i(j)}(S_i) \right] \frac{1}{\psi_j^2} + \frac{1}{\xi_k^2} \psi_j^2 \right\} \right) \end{aligned} \quad (\text{S10})$$

Where the term $\left| \frac{1}{2}(\psi_j^2)^{-1/2} \right|$ is the Jacobian of the transformation. It follows from this that

$$\pi(\psi_j^2 | d_j = k, \cdot) = GIG\left(\mathbf{a} = \frac{1}{\xi_k^2}, \mathbf{b} = \sum_{i=1}^N \boldsymbol{\eta}_{i(j)}(S_i)^T [D_w(W_i) - \phi W_i] \boldsymbol{\eta}_{i(j)}(S_i), \mathbf{c} = \frac{-S}{2} + \frac{1}{2}\right)$$

Thus, while the prior is specified in terms of the standard deviation ψ_j , in practice the sampling is performed on the variance ψ_j^2 . However, due to the simple monotonic relationship between the two quantities, this does not pose any practical inconvenience.

Random Effect Selection Indicators For each random effect selection indicator d_j , $j = 1, \dots, p$, each d_j once again takes on the value 0 or 1. Analogous to the main effect case, given prior $P(d_j = k) = p_{d,k}$, we have $P(d_j = k | \cdot) \propto \pi(\psi_j | d_j = k) p_{d,k}$. Once again, more concretely this comes to

$$P(d_j = k | \cdot) = \frac{\frac{1}{\sqrt{2\pi\xi_k^2}} \exp\left(\frac{-1}{2\xi_k^2} \psi_j^2\right) p_{d,k}}{\frac{1}{\sqrt{2\pi\xi_k^2}} \exp\left(\frac{-1}{2\xi_k^2} \psi_j^2\right) p_{d,0} + \frac{1}{\sqrt{2\pi\xi_k^2}} \exp\left(\frac{-1}{2\xi_k^2} \psi_j^2\right) p_{d,1}}$$

Random Effect Selection Probability Analogously to the main effect group, the final term in the main effect group is the random effect selection probability term, P_d . This term is entirely analogous to the P_γ term as outlined in S3.3.1. For completeness, the full conditional distribution of P_d is specified as follows:

$$\pi(P_d | \cdot) = \text{Beta}\left(1 + \sum_{j=1}^p d_j, 1 + \left[p - \sum_{j=1}^p d_j\right]\right)$$

S3.3.3 Error terms

Global CAR Process Variance By definition of τ^2 , the full conditional is given by

$$\pi(\tau^2 | \cdot) \propto \pi(\boldsymbol{\delta}_1, \dots, \boldsymbol{\delta}_N | \cdot) \pi(\tau^2)$$

Because $\boldsymbol{\delta}_i(S_i) \sim MVN(0, \tau^2 [D_w(W_i) - \rho W_i]^{-1})$, and $\tau^2 \sim InvGamma(a_\tau, b_\tau)$, by basic algebraic manipulation and properties of the determinant the equation above can be expressed as

$$\pi(\tau^2 | \cdot) \propto (\tau^2)^{-S/2-a_\tau} \exp\left(\frac{1}{\tau^2} \left[-\frac{1}{2} \sum_{i=1}^N (\boldsymbol{\delta}_i(S_i))^T [D_w(W_i) - \rho W_i] \boldsymbol{\delta}_i(S_i) + b_\tau\right]\right)$$

Thus,

$$\pi(\tau^2 | \cdot) = \text{InvGamma}(a_\tau + \frac{S}{2} + 1, \frac{1}{2} \sum_{i=1}^N (\boldsymbol{\delta}_i(S_i))^T [D_w(W_i) - \rho W_i] \boldsymbol{\delta}_i(S_i) + b_\tau)$$

Global CAR Process Correlation In order to improve the computational efficiency of sampling, a grid prior was placed on the correlation of the global CAR process, ρ . Given a discrete set of values and corresponding probabilities, v_1, \dots, v_K , and p_1, \dots, p_K , the full conditional probability that ρ is equal to v_k is given by:

$$\begin{aligned} P(\rho = v_k | \cdot) &\propto \left[\prod_{i=1}^N \pi(\boldsymbol{\delta}_i(S_i) | \rho, \tau^2) \right] \pi(\rho = v_k) \\ &\propto \left[\prod_{i=1}^N |(D_w(W_i) - v_k W_i)^{-1}|^{-1/2} \right] \exp\left(-\frac{1}{2\tau^2} \left[\sum_{i=1}^N \boldsymbol{\delta}_i(S_i)^T (D_w(W_i) - v_k W_i) \boldsymbol{\delta}_i(S_i) \right]\right) p_j \end{aligned} \quad (\text{S11})$$

It follows trivially from this that

$$P(\rho = v_k | \cdot) = \frac{\left[\prod_{i=1}^N |(D_w(W_i) - v_k W_i)^{-1}|^{-1/2} \right] \exp\left(-\frac{1}{2\tau^2} \left[\sum_{i=1}^N \boldsymbol{\delta}_i(S_i)^T (D_w(W_i) - v_k W_i) \boldsymbol{\delta}_i(S_i) \right]\right) p_j}{\sum_{t=1}^K \left[\prod_{i=1}^N |(D_w(W_i) - v_t W_i)^{-1}|^{-1/2} \right] \exp\left(-\frac{1}{2\tau^2} \left[\sum_{i=1}^N \boldsymbol{\delta}_i(S_i)^T (D_w(W_i) - v_t W_i) \boldsymbol{\delta}_i(S_i) \right]\right) p_t}$$

In practice, sampling from this distribution is accomplished using the so-called Gumbel Max trick; see section S3.1 for details and derivation.

Pure Error Variance Denoting $\varepsilon_{ij} = Y_{ij} - \mu_{ij}$, and $\boldsymbol{\varepsilon} = [\varepsilon_{11}, \dots, \varepsilon_{1n_1}, \dots, \varepsilon_{N1}, \dots, \varepsilon_{Nn_N}]^T$, it follows trivially from the specification of the model that

$$\boldsymbol{\varepsilon} \sim \text{MVN}(0, \nu^2 I) \quad (\text{S12})$$

Combined with the fact that $\nu^2 \sim \text{InvGamma}(a_\nu, b_\nu)$, it trivially follows from the conjugacy of the prior that

$$\pi(\nu^2 | \cdot) = \text{InvGamma}(a_\nu + \frac{S}{2}, b_\nu + \sum_{i=1}^N \sum_{j=1}^{n_i} \varepsilon_{ij}^2) \quad (\text{S13})$$

S3.4 Selected Genes

Table S3 shows the genes selected by the model, as well as which of the fixed- or random-effects were selected. For details on the gene composition of the combined gene sets (denoted by *), see Table S2.

Table S3: **Genes selected by model.** Genes selected by model, sorted by effect selection, along with which effect was selected (fixed, random, or both).

Gene	Cell Type	Fixed Effect Selected	Random Effect Selected
ITGAX	Macrophage	✓	
MAN2B1	Macrophage	✓	
NR1H3	Macrophage	✓	
SLC31A2	Macrophage	✓	
GRN	Monocyte	✓	
HMOX1	Monocyte	✓	
VCAN	Monocyte	✓	
KIR3DL2	NK		✓
KLRC4	NK	✓	✓
NK_2*	NK	✓	
AQP9	Neutrophil	✓	
BCL6	Neutrophil	✓	
CD97	Neutrophil		✓
CFLAR	Neutrophil	✓	
FAM65B	Neutrophil	✓	✓
Neutrophil_1*	Neutrophil	✓	
GLT1D1	Neutrophil		✓
GPR97	Neutrophil		✓
IFITM2	Neutrophil		✓
KCNJ2	Neutrophil		✓
KIAA0247	Neutrophil	✓	
LIMK2	Neutrophil		✓
MGAM	Neutrophil		✓
NAMPT	Neutrophil		✓
PHF21A	Neutrophil		✓
PLXNC1	Neutrophil	✓	✓
Neutrophil_2*	Neutrophil		✓
STAT5B	Neutrophil		✓
TMEM154	Neutrophil		✓
Plasma_1*	Plasma	✓	✓
TXNDC5	Plasma		✓
FYN	T		✓
T_1*	T	✓	
IL23A	T		✓
PRKCH	T		✓

S3.5 Model Trace Plots

The Geweke Diagnostic was used to assess convergence in the application model. Figure S2 shows trace plots from the overall log-likelihood of the model as well as selected fixed- and random-effect parameters.

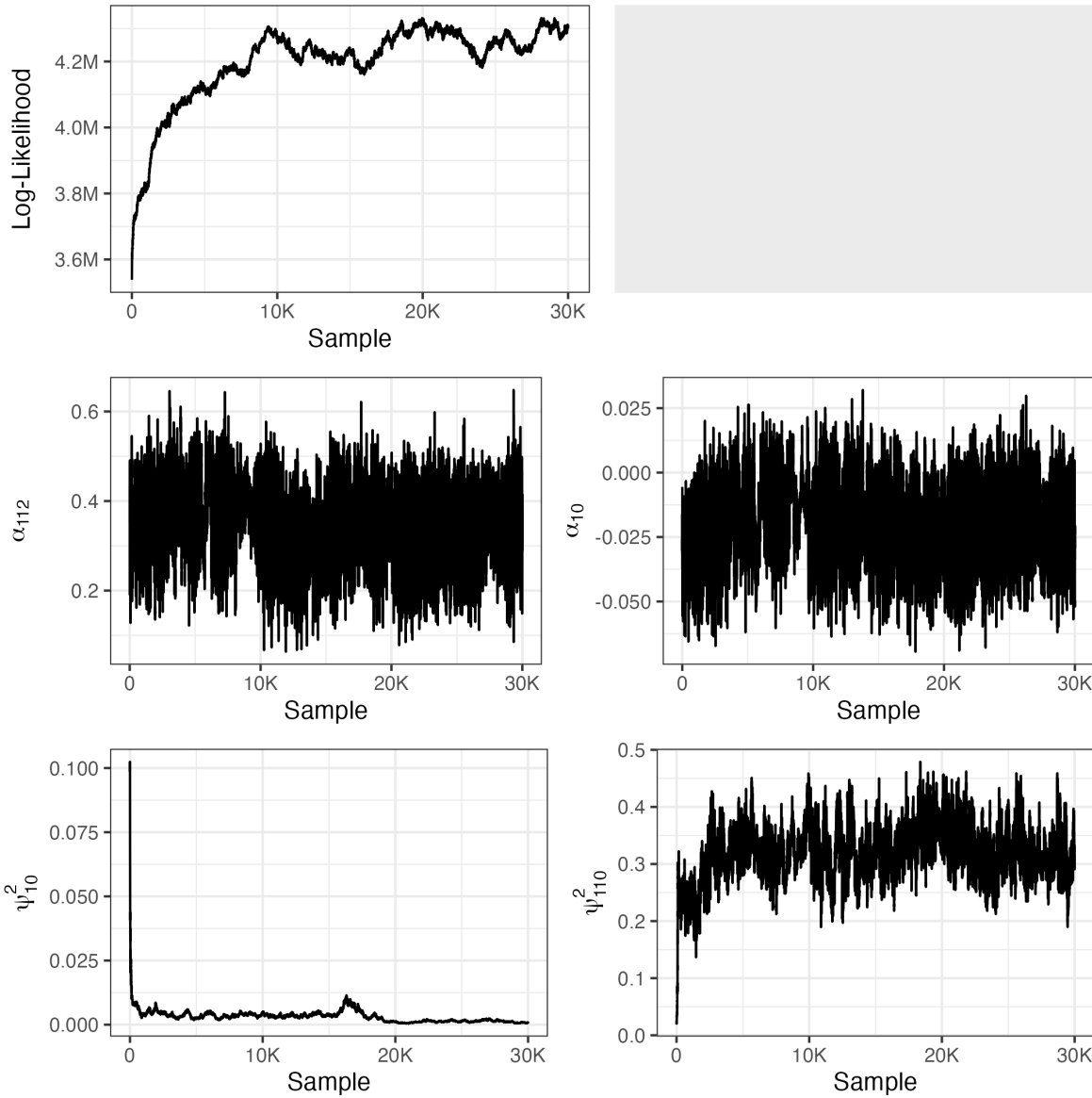


Figure S2: **Trace plots from application fitting.** Trace plots from the log-likelihood and various parameters of the application model fitting.

References

Osher, N., Kang, J., Krishnan, S., Rao, A., and Baladandayuthapani, V. (2023). Spartin: a bayesian method for the quantification and characterization of cell type interactions in spatial pathology data. *Frontiers in Genetics*.